

Probing the Heights and Depths of Y Dwarf Atmospheres: A Retrieval Analysis of the JWST Spectral Energy Distribution of WISE J035934.06–540154.6

HARSHIL KOTHARI,¹ MICHAEL C. CUSHING,¹ BEN BURNINGHAM,² SAMUEL A. BEILER,¹ J. DAVY KIRKPATRICK,³
ADAM C. SCHNEIDER,⁴ SAGNICK MUKHERJEE,⁵ AND MARK S. MARLEY⁶

¹*Ritter Astrophysical Research Center, Department of Physics & Astronomy, University of Toledo, 2801 W. Bancroft St., Toledo, OH 43606, USA*

²*Centre for Astrophysics Research, School of Physics, Astronomy and Mathematics, University of Hertfordshire, Hatfield AL10 9AB*
³*IPAC, Mail Code 100-22, Caltech, 1200 E. California Boulevard, Pasadena, CA 91125, USA*

⁴*United States Naval Observatory, Flagstaff Station, 10391 West Naval Observatory Road, Flagstaff, AZ 86005, USA*

⁵*Department of Astronomy and Astrophysics, University of California, Santa Cruz, 1156 High Street, Santa Cruz, CA 95064, USA*

⁶*Lunar and Planetary Laboratory, University of Arizona, 1629 E. University Boulevard, Tucson, AZ 85721, USA*

ABSTRACT

We present an atmospheric retrieval analysis of the Y0 brown dwarf WISE J035934.06–540154.6 using the low-resolution 0.96–12 μm JWST spectrum presented in [Beiler et al. \(2023\)](#). We obtain volume number mixing ratios of the major gas-phase absorbers (H_2O , CH_4 , CO , CO_2 , PH_3 , and H_2S) that are 3–5 \times more precise than previous work that used HST spectra. We also find an order-of-magnitude improvement in the precision of the retrieved thermal profile, a direct result of the broad wavelength coverage of the JWST data. We used the retrieved thermal profile and surface gravity to generate a grid of chemical forward models with varying metallicity, $(\text{C}/\text{O})_{\text{atm}}$, and strengths of vertical mixing as encapsulated by the eddy diffusion coefficient K_{zz} . Comparison of the retrieved abundances with this grid of models suggests that the deep atmosphere of WISE 0359–54 shows signs of vigorous vertical mixing with $K_{\text{zz}} = 10^9 \text{ [cm}^2 \text{ s}^{-1}\text{]}$. To test the sensitivity of these results to our 5-knot spline thermal profile model, we performed a second retrieval using the [Madhusudhan & Seager \(2009\)](#) thermal profile model. While the results of the two retrievals generally agree well, we do find differences between the retrieved values of mass and volume number mixing ratio of H_2S with fractional differences of the median values of -0.64 and -0.10 , respectively. In addition, the 5-knot thermal profile is consistently warmer at pressure between 1 and 70 bar. Nevertheless, our results underscore the power that the broad-wavelength infrared spectra obtainable with the James Webb Space Telescope have to characterize the atmospheres of cool brown dwarfs.

Keywords: stars: abundances(1577), stars: atmosphere(1584, 2309), (stars:) brown dwarfs(185), stars: statistics(1900), radiative transfer(1335)

1. INTRODUCTION

In the last decade, atmospheric retrieval, a method by which the properties of an atmosphere are inferred directly from an observed spectrum, has become a powerful technique for studying the atmospheres of both brown dwarfs and exoplanets (e.g., [Madhusudhan & Seager 2009](#); [Line et al. 2014](#)). With roots in the study of the planets in our solar system (e.g., [Chahine 1968](#)), a retrieval determines the thermal profile (i.e. the run of temperature and pressure) and atomic/molecular abundances of an atmosphere by iteratively comparing tens of thousands of model spectra to observations in order to optimize the model parameters.

Previous retrievals of brown dwarfs have mostly focused on the warmer objects that populate the L and T spectral classes ([Line et al. 2014](#); [Burningham et al. 2017](#); [Zalesky et al. 2019](#); [Lueber et al. 2022](#); [Adams et al. 2023](#); [Rowland et al. 2023](#); [Vos et al. 2023](#); [Hood et al. 2024](#)). These retrievals use relatively broad-wavelength spectra covering a minimum of the 0.8–2.4 μm wavelength and often extending to 4–5 μm or even to $\sim 15 \mu\text{m}$.

The cooler brown dwarfs that populate the Y spectral class are rare (roughly 50 are known), faint ($M_{\text{H}} \gtrsim 21 \text{ mag}$), and emit-most of their radiation at mid-infrared wavelengths. As a result, the majority of retrievals that

have been performed on them used spectra with limited wavelength coverage and/or signal-to-noise ratio. [Zalesky et al. \(2019\)](#) performed retrievals of 8 Y dwarfs using low-resolution 1–1.7 μm Hubble Space Telescope spectra ([Schneider et al. 2015](#)) and measured the abundances of H_2O , CH_4 , NH_3 , and upper limits for the abundances of CO and CO_2 . The H_2O and CH_4 abundances were consistent with the predictions of thermochemical equilibrium models, but [Zalesky et al.](#) suggested that the abundance of NH_3 may be affected by vertical mixing within the atmosphere. Unfortunately the narrow wavelength coverage of the HST spectra limit the precision with which the abundances and the thermal profiles can be measured (uncertainties of ~ 0.14 dex and ~ 200 K, respectively) because they only probe a relatively narrow range of pressures in the atmosphere.

The launch of the James Webb Space Telescope (hereafter JWST; [Gardner et al. 2006](#)) has opened a new frontier in the study of Y dwarfs because low- and moderate-resolution spectra are now available over the 1 to 28 μm wavelength range. [Barrado et al. \(2023\)](#) used several retrieval codes to detect both $^{14}\text{NH}_3$ and $^{15}\text{NH}_3$ in the moderate-resolution 4.9–18 μm spectrum of WISEP J182831.08+265037.8 (hereafter WISE 1828+25; $T_{\text{eff}} \approx 350$ K) and found a $^{14}\text{N}/^{15}\text{N}$ value of 673_{-212}^{+393} , consistent with formation by gravitational collapse of a molecular cloud. [Lew et al. \(2024\)](#) used a moderate-resolution 2.88–5.12 μm spectrum of WISE 1828+26 to obtain abundances of H_2O , CH_4 , CO_2 , NH_3 , H_2S and measured a C/O value of 0.45 ± 0.01 .

In this paper, we add to the short list of brown dwarf JWST-based retrievals by presenting a retrieval analysis of WISE J035934.06–540154.6 (hereafter WISE 0359–54) using the low-resolution 0.96–12 μm JWST spectrum presented in [Beiler et al. \(2023\)](#). WISE 0359–54 has a spectral type of Y0, lies at a distance of 13.57 ± 0.37 pc ($\varpi_{\text{abs}} = 73.6 \pm 2.0$ mas, [Kirkpatrick et al. 2021](#)), and has an effective temperature (T_{eff}) of 467_{-18}^{+16} K ([Beiler et al. 2023](#)). In §2, we will briefly discuss the spectrum being used for this analysis. In §3, we will discuss the retrieval framework that is used to perform the retrieval analysis for WISE 0359–54. In §4, we will present and discuss the retrieved results. Finally, in §5, we will summarize and point out key findings of this retrieval analysis.

2. THE SPECTRUM

We analyzed the 0.96–12 μm JWST spectrum of the Y0 dwarf WISE 0359–54 presented in [Beiler et al. \(2023\)](#). The spectrum was obtained using the Near Infrared Spectrograph (hereafter NIRSpec, [Jakobsen et al. 2022](#)), which covers 0.6–5.3 μm , and the Mid-Infrared

Instrument (hereafter MIRI, [Rieke et al. 2015](#)), which covers 5–12 μm . The resolving power of the spectra are strong functions of wavelength but on average are $R \equiv \lambda/\Delta\lambda \approx 200$. [Beiler et al.](#) used Spitzer/IRAC Channel 2 ([4.5]) photometry from [Kirkpatrick et al. \(2012\)](#) and MIRI F1000W ($\lambda_{\text{pivot}} = 9.954$ μm) photometry to absolutely flux calibrate the NIRSpec and MIRI spectra to an overall precision of $\sim 5\%$. [Beiler et al.](#) then created a continuous 0.96–12 μm spectrum by merging the NIRSpec and the MIRI spectrum between 5 and 5.3 μm , where the spectra overlapped. The 0.96–12 μm spectrum is shown in Figure 1 in units of f_λ along with the locations of prominent molecular absorption bands of H_2O , CH_4 , CO , CO_2 , and NH_3 identified by [Beiler et al.](#)

3. THE METHOD

We use the Brewster retrieval framework ([Burningham et al. 2017](#)) for our analysis. We assume that each datum in the spectrum is generated from the following probabilistic model,

$$F_\lambda(\lambda_i) = (R/d)^2 [\mathbf{I}(\lambda_i) * \mathcal{F}_\lambda(\boldsymbol{\theta}_{\text{atm}}, \lambda_j)] + \epsilon(\lambda_i), \quad (1)$$

where $F_\lambda(\lambda_i)$ is a random variable giving the flux density of the spectrum at the i th wavelength λ_i , R is the radius of the brown dwarf, d is the distance of the brown dwarf, $\mathbf{I}(\lambda_i)$ is the instrument profile at λ_i , the asterisk denotes a convolution, \mathcal{F}_λ is a model emergent flux density at the surface of the brown dwarf, $\boldsymbol{\theta}_{\text{atm}}$ is a vector of parameters describing the atmospheric model, λ_j is equal to $\lambda_k + \Delta\lambda$, where λ_k is the wavelength at which the model emergent flux is calculated and $\Delta\lambda$ is a parameter that accounts for any wavelength uncertainty, and $\epsilon(\lambda_i)$ is a random variable that is distributed as a Gaussian with a mean of zero and a variance of $\sigma(\lambda_i)^2$. We further assume the variances $\sigma^2(\lambda_i)$ are given by,

$$\sigma^2(\lambda_i) = s^2(\lambda_i) + 10^b, \quad (2)$$

where $s_i(\lambda_i)$ is the standard error of the spectrum at λ_i and b is a tolerance parameter that is used to inflate the measured uncertainties to account for unaccounted sources of uncertainty (e.g., [Hogg et al. 2010](#); [Foreman-Mackey et al. 2013](#); [Burningham et al. 2017](#)).

The one-dimensional atmospheric model is divided into 64 layers (65 levels), with the pressure ranging from 10^{-4} to $10^{2.3}$ bar, in steps of 0.1 dex. This range was chosen based on the pressure regions that can be probed with the spectrum being used for this retrieval analysis and the available opacities. For simplicity we assume the atmosphere is cloudless and so the only sources of opacity are the absorbing gases H_2 , He, H_2O , CH_4 , CO , CO_2 ,

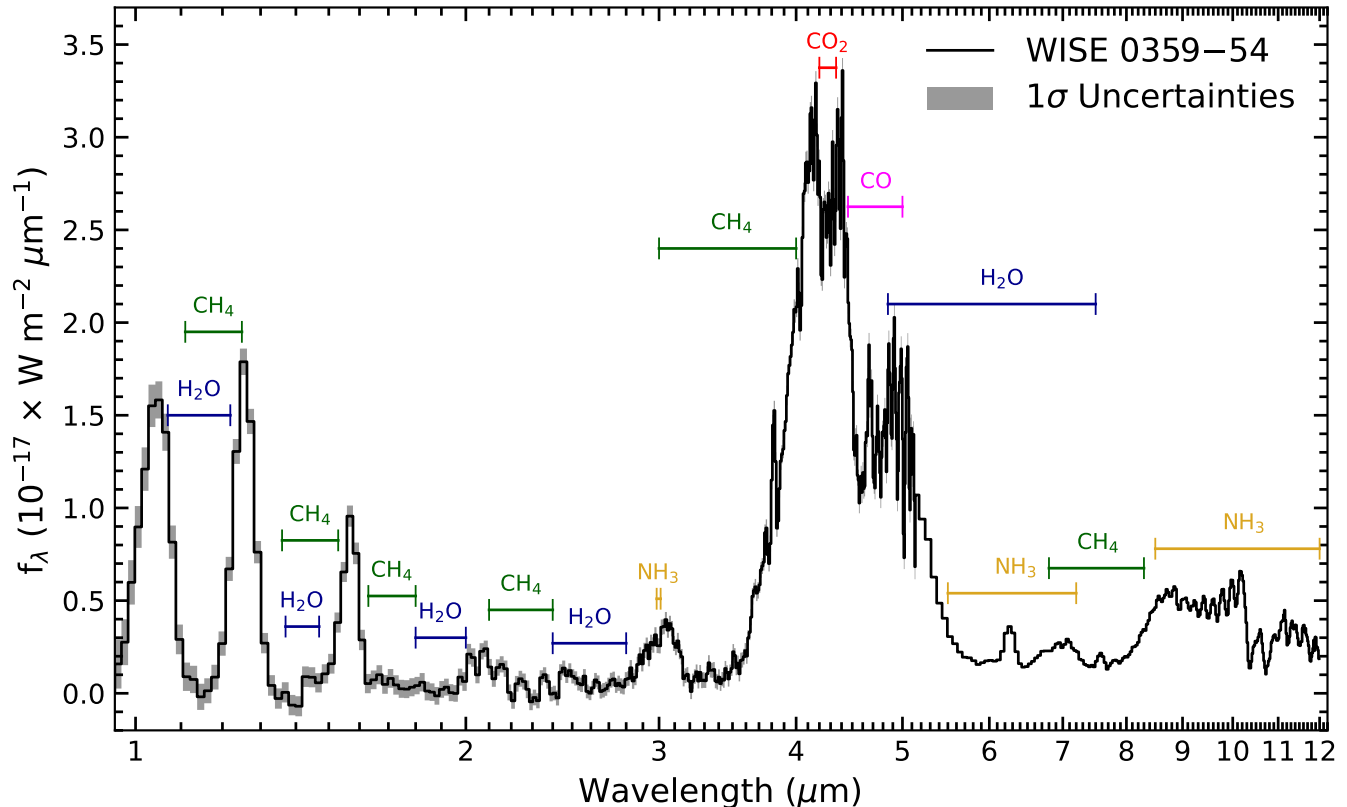


Figure 1. The 0.96–12 μm JWST spectrum with 1σ uncertainties (NIRSpec + MIRI LRS) of WISE 0359–54 spectrum (Beiler et al. 2023) in units of f_λ . The typical signal-to-noise of the NIRSpec and MIRI LRS spectra are ~ 20 and ~ 100 , respectively. Also plotted are the locations of prominent absorption bands of H₂O, CH₄, CO, CO₂, and NH₃.

NH₃, H₂S, K, Na, and PH₃. H₂ and He contribute a continuum opacity in the form of collision-induced absorption (i.e. H₂-H₂, H₂-CH₄, and H₂-He). The uniform-with-altitude volume number mixing ratios¹ (hereafter mixing ratios) of the remaining molecules are free parameters. The thermal profile is modeled with a 5-knot interpolating spline in which the knots are located at the top ($T_{\text{Knot } 1}$), middle ($T_{\text{Knot } 3}$) and bottom ($T_{\text{Knot } 5}$) of the atmosphere, with one point halfway between the top and the middle ($T_{\text{Knot } 2}$) of the atmosphere, and one point halfway between the bottom and the middle ($T_{\text{Knot } 4}$) of the atmosphere. The mass and radius of the brown dwarf are also free parameters which are then used to calculate the surface gravity ($g = GM/R^2$). Taken together, the parameters for the mixing ratios of the 9 gas species, the 5 parameters for the thermal profile, and mass and radius make up θ_{atm} in Equation 1.

¹ The volume number mixing ratio of a species is the number density of that species divided by the total number density of the gas.

For a given θ_{atm} , the emergent spectrum at the top of the atmosphere \mathcal{F}_λ is calculated by using a two-stream source function technique from Toon et al. (1989). The emergent spectrum is then convolved with the instrument profile $I(\lambda_i)$, which we assume is a Gaussian, to account for the variable resolving power of the data (see Beiler et al. (2023) for further discussion on this latter process).

If we let, $\Theta = \{\theta_{\text{atm}}, d, b, \Delta\lambda\}$ then we can use Bayes' Theorem to calculate the posterior probability density function for the parameters Θ given the data \mathbf{f}_λ ,

$$p(\Theta|\mathbf{f}_\lambda) = \frac{p(\Theta)\mathcal{L}(\mathbf{f}_\lambda|\Theta)}{p(\mathbf{f}_\lambda)}, \quad (3)$$

where $p(\Theta)$ is the prior probability for the set of parameters, $\mathcal{L}(\mathbf{f}_\lambda|\Theta)$ is the likelihood that quantifies the probability of the data given the model, and $p(\mathbf{f}_\lambda)$ is the Bayesian evidence. If we let

$$\mathcal{M}_\lambda(\lambda_i) = (R/d)^2[I(\lambda_i) * \mathcal{F}_\lambda(\theta_{\text{atm}}, \lambda_j)], \quad (4)$$

then the natural logarithm of the likelihood function is given by,

$$\ln \mathcal{L}(\mathbf{f}_\lambda | \Theta) = -\frac{1}{2} \sum_{i=1}^n \left\{ \frac{[f_{\lambda,i} - \mathcal{M}_\lambda(\lambda_i)]^2}{\sigma(\lambda_i)^2} - \ln[2\pi\sigma(\lambda_i)^2] \right\}, \quad (5)$$

because we assume that the data are independent and $\epsilon(\lambda)$ is distributed as a Gaussian. The prior distributions for each of the 19 parameters are given in Table 1.

To explore the posterior parameter space, we use the nested sampling version of the Brewster, which uses PyMultiNest (Buchner et al. 2014). PyMultiNest is initialized to sample the parameter space with 500 live points for 19 free parameters. The calculation was done using the Owens cluster (Center 2016) at the Ohio Supercomputer Center (Center 1987). The sampling is complete when the change in the natural logarithm of the evidence is less than 0.5 (for a deeper discussion see Feroz et al. 2009; Speagle 2020).

4. RESULTS & DISCUSSION

The result of solving Bayes' theorem is a joint posterior distribution for the 19 parameters. In the Appendix, Figure 12 shows the marginalized posterior probability distributions for all 19 parameters using equally weighted posterior samples generated by PyMultiNest and Table 3 gives the median, and 1σ uncertainty for each of the parameters. In the following sections, we discuss the values of these parameters in more detail.

4.1. The Thermal Profile

The first panel in Figure 2 shows the retrieved thermal profile; the black solid line shows the median (50th percentile) profile (calculated using the median values of the retrieved parameters) and the red shaded region represents the 16th and 84th percentile (1σ central credible interval²), and 2.4th and 97.6th percentile (2σ central credible interval). Also plotted are a subset of normalized contribution functions at wavelengths covering the 0.96–12 μm wavelength range; those in grey are the wavelengths covered by HST/WFC3 spectra ($\lambda < 1.7\mu\text{m}$) while the blue cover the wavelengths longward of 1.7 μm . Integration of a contribution function over (log) pressure in a semi-infinite atmosphere gives the specific intensity at the top of the atmosphere at the corresponding wavelength (Chamberlain & Hunten

1987). A normalized contribution function therefore indicates the layers of the atmospheres from which light at that wavelength emerges. The opacity windows centered at the *J*- and *H*-bands probe deep, hotter layers of the atmosphere (grey lines) while longer wavelengths generally probe higher and cooler layers of the atmosphere (blue lines). The handful of contribution functions at pressure lower than 10^{-2} bar come primarily from the 6.3–7.8 μm wavelength range. The JWST spectrum therefore probes nearly four orders of magnitude in pressure; two more than previous work (Zalesky et al. 2019) using HST spectra alone. In addition, the median width of the 1σ central credible interval is ~ 20 K which is an order of magnitude lower than typically found using HST spectra alone (Zalesky et al. 2019).

A cloudless self-consistent 1D radiative-convective equilibrium Sonora Elf Owl thermal profile with solar metallicity and C/O ratio (green dashed line, Mukherjee et al. 2024) is also plotted in the first panel of Figure 2. The effective temperature and (log) surface gravity of 450 K and 4.5 [cm s^{-2}] were chosen to match our derived values of 458 K and 4.46 [cm s^{-2}] (see §4.4) as closely as possible. The difference between the two profiles are shown in the second panel of Figure 2. Overall, the retrieved profile matches the self-consistent profile well, although the retrieved profile is systematically hotter by up to 100 K between 0.01 and 10 bars and systematically cooler by up to 500 K in the deepest layers of the atmosphere. The retrieved profile also shows a slight temperature reversal of ~ 30 K at the top of the atmosphere. While this is probably unphysical, Faherty et al. (2024) did identify CH_4 emission in the moderate-resolution JWST spectrum of the Y dwarf CWISEP J193518.59–154620.3 at 3.326 μm . They modelled this as a 300 K temperature reversal between the 1 and 10 millibar pressure range and so further investigation into our reversal is warranted.

In order to investigate the possibility that the differences between the retrieved profile and Elf Owl profile are due to an inability of the 5-knot spline to reproduce the shape of the Elf Owl profile, we have fitted the Elf Owl profile with a 5-knot spline and the results are shown in the third panel of Figure 2; the difference between the two profiles is shown in the last panel. The Elf Owl profile does not extend up to the 10^{-4} bar level so we placed the top knot at $10^{-3.7}$ bar, the vertical extent of the Elf Owl profile. The 5-knot spline easily reproduces the Elf Owl profile with a root mean squared deviation of 17 K and a maximum deviation of < 50 K. This indicates that the differences between the retrieved profile and the Elf Owl profile are real and statistically significant.

² A Bayesian central credible interval gives the range of values in a parameter's posterior distribution that contain $\alpha\%$ of the probability. In contrast, a frequentist $\alpha\%$ confidence interval means that $\alpha\%$ of a large number of confidence intervals computed in the same way would contain the true value of the parameter.

Table 1. Parameters Priors

Parameter	Prior ^a
Gas Volume Mixing Ratio $\log(f_i)$ ^{b,c}	$\mathcal{U}(-12, \infty), \sum_{i=1}^9 f_i \leq 1$
Mass M ($\mathcal{M}_{\text{Jup}}^{\text{N}}$)	$\mathcal{U}(1, 80)$
Radius R ($\mathcal{R}_{e,J}^{\text{N}}$)	$\mathcal{U}(0.5, 2)$
Wavelength Shift $\Delta\lambda$ (μm)	$\mathcal{U}(-0.01, 0.01)$
Tolerance Factor b	$\mathcal{U}(10^{0.01} \times \min(\sigma_i^2), 10^{100} \times \max(\sigma_i^2))$
5-Knot Thermal Profile: $T_{\text{Knot } i}$ (K)	$\mathcal{U}(0, 5000)$
Madhusudhan & Seager Thermal Profile: $\alpha_1, \alpha_2, P_1, P_3, T_3$	$\mathcal{U}(0.25, 0.5), \mathcal{U}(0.1, 0.2), \mathcal{U}(10^{-4}, 10^{2.3}), \mathcal{U}(10^{-4}, 10^{2.3}), \mathcal{U}(0, 5000)$
Distance d (pc)	$\mathcal{N}(13.57, 0.37^2)$

^a $\mathcal{U}(\alpha, \beta)$ denotes a uniform distribution between α and β while $\mathcal{N}(\mu, \sigma^2)$ denotes a normal distribution with a mean of μ and a variance of σ^2 .

^bWe included H_2O , CH_4 , CO , CO_2 , NH_3 , H_2S , K , Na , PH_3 .

^cAll volume mixing ratios are reported as the log of the volume number mixing ratio (the number density of the species divided by the total number number density of the gas), where the remainder of the gas is assumed to be H_2 -He ($1 - \sum_i f_i$). Of the remainder gas 84% of the volume mixing ratio is from H_2 and 16% is from He, assuming a solar abundance of 91.2% of number of atoms of H and 8.7% of number of atoms of He (Asplund et al. 2009).

4.2. Retrieved Model Spectrum

Figure 3 shows the JWST spectrum of WISE 0359–54 along with the retrieved median model spectrum (upper panel) and the residual (O-C, lower panel). The model spectrum is generated using the median thermal profile and the 1σ central credible interval is generated using the 1σ of the 5-knot thermal profile. Overall, the model fits the data well as the residuals are mostly random. However, the model fails to reproduce the observations in the 1–2 μm range. The poor agreement shortward of 1.1 μm is likely a result of our poor understanding of the exact shape of the pressure-broadened wings of the resonant K I and Na I doublets at 7665/7699 \AA and 8183/8195 \AA , respectively (see Burningham et al. (2017) for a more in-depth discussion).

4.3. Mixing Ratios

Figure 4 shows the marginalized posterior probability distributions for the mixing ratios of H_2O , CH_4 , CO , CO_2 , NH_3 , and H_2S . With secure detections of all the dominant carbon- and oxygen-bearing molecules, we can also calculate the atmospheric $(\text{C}/\text{O})_{\text{atm}}$ ratio as

$$(\text{C}/\text{O})_{\text{atm}} = \frac{f_{\text{CO}} + f_{\text{CO}_2} + f_{\text{CH}_4}}{f_{\text{H}_2\text{O}} + f_{\text{CO}} + 2f_{\text{CO}_2}}. \quad (6)$$

and so Figure 4 also shows the marginalized posterior probability distribution for $(\text{C}/\text{O})_{\text{atm}}$ calculated using the samples of f_{CO} , f_{CO_2} , f_{CH_4} , and $f_{\text{H}_2\text{O}}$. It should be noted that $\sim 20\%$ of oxygen is depleted due to the sequestration of oxygen in condensates like enstatite (MgSiO_3)

and forsterite (MgSi_2O_4) (Lodders & Fegley 2002) which would bring the median bulk $(\text{C}/\text{O})_{\text{bulk}}$ to 0.658.

In order to perform a sanity check on our retrieved abundances and $(\text{C}/\text{O})_{\text{atm}}$ ratio, we compare our values to those reported by Zalesky et al. (2019) for 8 Y dwarfs, and Barrado et al. (2023) and Lew et al. (2024) for the archetype Y dwarf WISE 1828+26 in Table 2. We note that the Barrado et al. uncertainties are an order-of-magnitude larger than the other works because they were computed by combining (with equal weight) the posterior distributions from five different retrieval analyses.

In general, the mixing ratio and $(\text{C}/\text{O})_{\text{atm}}$ values agree well. The mixing ratios of H_2O and NH_3 fall within the range of values found by Zalesky et al. (2019) but the values for CH_4 and $(\text{C}/\text{O})_{\text{atm}}$ fall towards the lower and upper limits of the ranges, respectively. Our values and those of Lew et al. (2024) are inconsistent given the uncertainties; however this could be because WISE 1828+26 is 110 K cooler than WISE 0359–54 and/or because both sets of measurements are likely dominated by systematic uncertainties not accounted for in the respective analyses (see §4.6). The Barrado et al. values generally agree with our values, but this is more likely a result of their order-of-magnitude-larger uncertainties generated by combining the results of several retrieval analyses.

H_2S exhibits many rotation-vibrational bands in the 1–12 μm wavelength range centered at 1.33, 1.6, 2, 2.6, 4.0, and 8.0 μm . However, with the exception of a single absorption line detected at $\lambda=1.590$ μm

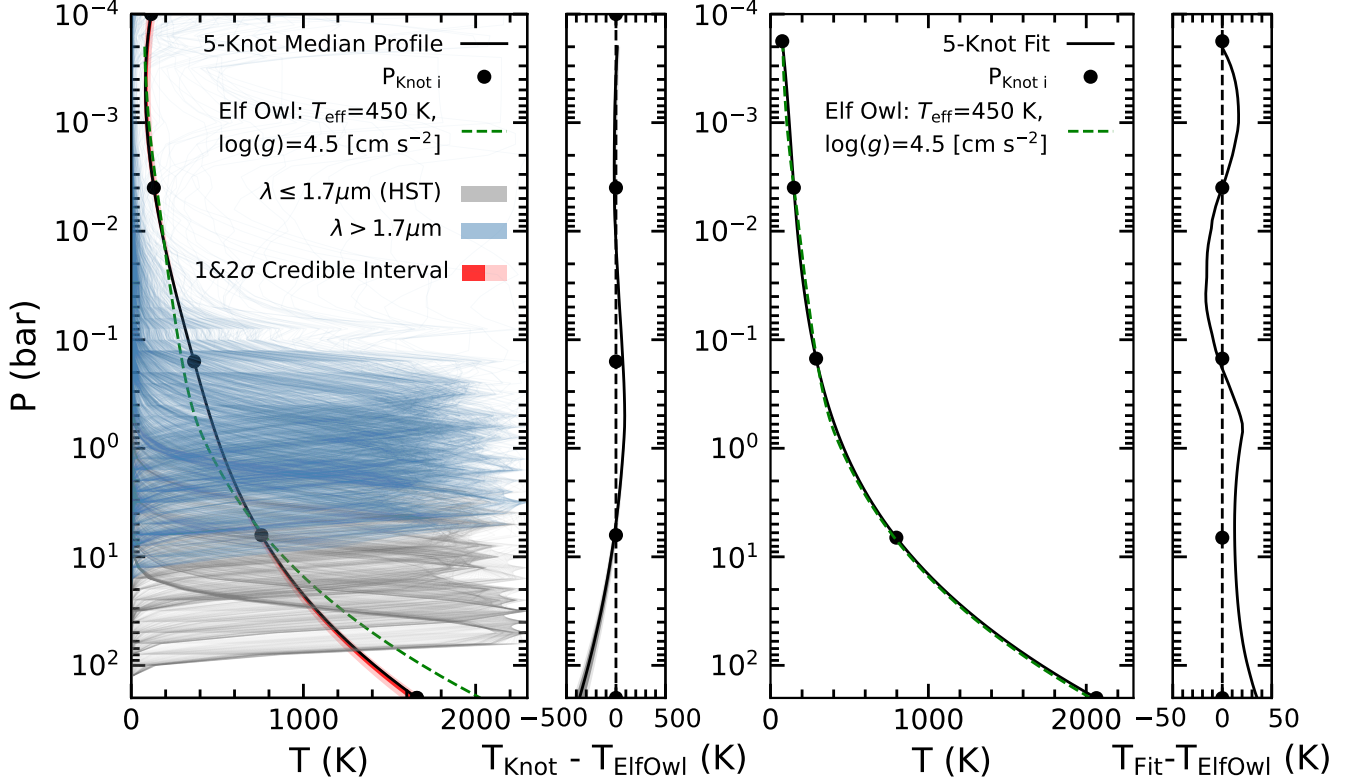


Figure 2. Left two panels (Retrieved vs. Forward Model): the black solid curve shows the 5-knot retrieved median thermal profile, the red region shows the 1 and 2 σ central credible interval around the median profile, and the green dashed curve is a solar metallicity, solar C/O ratio, cloudless Elf-Owl thermal profile with $T_{\text{eff}}=450$ K and $\log(g)=4.5$ [cm s^{-2}]. Also plotted are normalized contribution functions in gray (HST wavelength coverage, $\lambda \leq 1.7 \mu\text{m}$) and in blue ($\lambda > 1.7 \mu\text{m}$). The opacity windows centered at the J - and H -bands probe deep, hotter layers of the atmosphere while longer wavelengths general probe higher and cooler layers of the atmosphere. The handful of contributions functions at pressure lower than 10^{-2} bar come primarily from the 6.3–7.8 μm wavelength range. **Right two panels (Forward Model vs. Forward Model Fit):** the dashed green curve is the Elf-Owl thermal profile with a $T_{\text{eff}}=450$ K and $\log(g)=4.5$ cm s^{-2} and the black solid curve shows the 5-knot spline fit of the same Elf-Owl thermal profile. The black dots in all the panels represent the position of the 5 knots. **Note:** The temperature range in panel 2 is an order of magnitude larger than the range in panel 4.

in an $R \approx 45,000$ spectrum of the T6 dwarf 2MASS J08173001–6155158 (Tannock et al. 2022), spectral features of H_2S have remained undetected in the spectra of cool brown dwarfs. However, Hood et al. (2023) showed that a retrieval that includes H_2S as an opacity source produced a better fit to the moderate-resolution ($R \sim 6000$) near-infrared spectrum of the T9 dwarf UGPS J072227.51–054031.2 than a retrieval without H_2S opacity. Lew et al. also found that excluding H_2S opacity in their retrieval of WISE 1828+26 increased the χ^2 of the fit by over 900. These results suggest that retrievals can still detect H_2S in the atmospheres of cool brown dwarfs even though there are no obvious absorption features in their low- to moderate-resolution spectra. Lew et al. retrieved a mixing ratio of $-4.44^{+0.03}_{-0.03}$ for WISE 1828+26, which is 0.24 dex lower than our value. We note that these are the only two detections of H_2S in atmospheres of Y dwarfs and so a larger sample

of cool brown dwarfs will be required (Kothari et al., in prep) to determine whether this difference is significant or not.

Finally, we included PH_3 as a source of opacity in our retrieval because the best fitting Sonora model for WISE 0359–54 in Beiler et al. (2023) predicts the presence of phosphine. However, our retrieved mixing ratio of $-10.00^{+1.15}_{-1.26}$ is consistent with the lack of any PH_3 spectroscopic features (Beiler et al. 2023). The lack of PH_3 absorption bands in the spectra of the coolest brown dwarfs (down to ~ 250 K) (Miles et al. 2020; Luhman et al. 2023) remains an outstanding problem given that PH_3 has been detected in the spectra of Jupiter and Saturn (Gillett et al. 1973; Beer 1975; Bregman et al. 1975; Barshay & Lewis 1978).

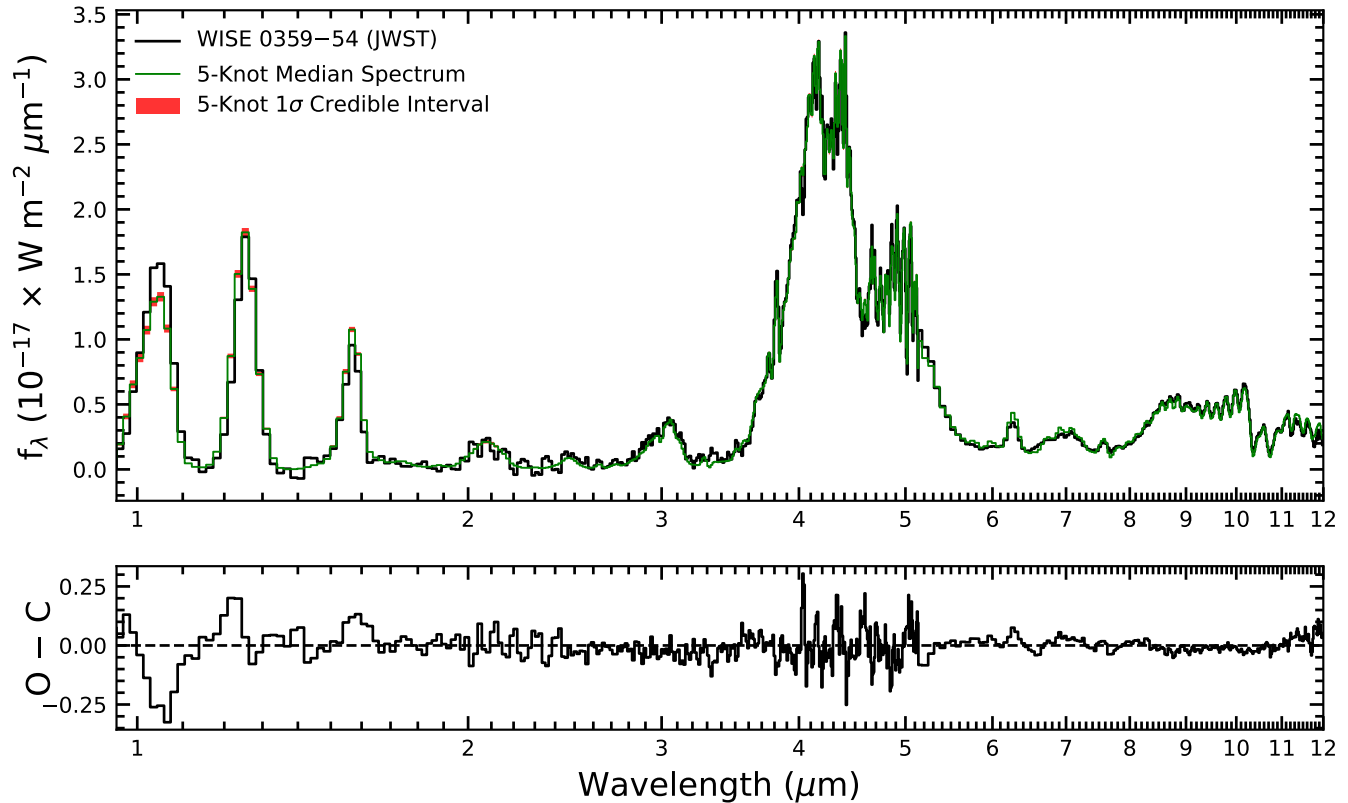


Figure 3. **Top panel:** shows the observed spectrum in black and the retrieved median spectrum from 5-knot retrieval in green for WISE 0359–54 spectrum covering 0.96–12 μ m. The red region show the 1σ central credible interval around the median spectrum. **Bottom panel:** shows the residual spectrum calculated by taking the difference between the retrieved median spectrum and the observed spectrum.

Table 2. Parametric Value Comparison

Parameter	W0359-54		8 Y dwarfs	WISE J1828+26	
	This Work		Zalesky et al. (2019)	Lew et al. (2024)	Barrado et al. (2023) ^a
	5-Knot	Parametrized	(min–max)		
$\log(f_{\text{H}_2\text{O}})$	$-3.13^{+0.03}_{-0.02}$	$-3.10^{+0.04}_{-0.04}$	$-2.68 - -3.32$	$-2.71^{+0.01}_{-0.02}$	$-3.03^{+0.18}_{-0.21}$
$\log(f_{\text{CH}_4})$	$-3.43^{+0.03}_{-0.03}$	$-3.34^{+0.04}_{-0.04}$	$-2.63 - -3.42$	$-3.07^{+0.01}_{-0.02}$	$-3.65^{+0.11}_{-0.21}$
$\log(f_{\text{CO}})$	$-5.19^{+0.03}_{-0.02}$	$-5.18^{+0.04}_{-0.04}$	$-3.3 - -4.2$ ^b
$\log(f_{\text{CO}_2})$	$-8.11^{+0.04}_{-0.03}$	$-8.05^{+0.05}_{-0.05}$	$-3.6 - -4.6$ ^b	$-8.79^{+0.03}_{-0.04}$...
$\log(f_{\text{NH}_3})$	$-4.59^{+0.04}_{-0.03}$	$-4.51^{+0.05}_{-0.05}$	$-4.11 - -4.84$	$-4.21^{+0.02}_{-0.02}$	$-4.79^{+0.15}_{-0.25}$
$\log(f_{\text{H}_2\text{S}})$	$-4.18^{+0.05}_{-0.05}$	$-4.60^{+0.12}_{-0.12}$	$-4.3 - -6.3$ ^b	$-4.44^{+0.03}_{-0.03}$...
C/O	$0.548^{+0.002}_{-0.002}$	$0.538^{+0.003}_{-0.002}$	$-0.55 - -1.10$	$0.45^{+0.01}_{-0.01}$	$0.21^{+0.45}_{-0.03}$

NOTE—^aAveraged retrieved results from 5 different retrieval codes.

^bThese ranges represent 3σ upper limit values.

Figure 5 shows a comparison of the mixing ratios for H₂O, CH₄, CO, CO₂, NH₃, and H₂S to the predictions of a thermochemical equilibrium model. The solid colored bars indicate the 1σ central credible interval for each

mixing ratio and the corresponding dashed line gives the model predictions which are calculated using chemical equilibrium grids generated using the NASA Gibbs minimization CEA code (see Fegley & Lodders 1994; Fe-

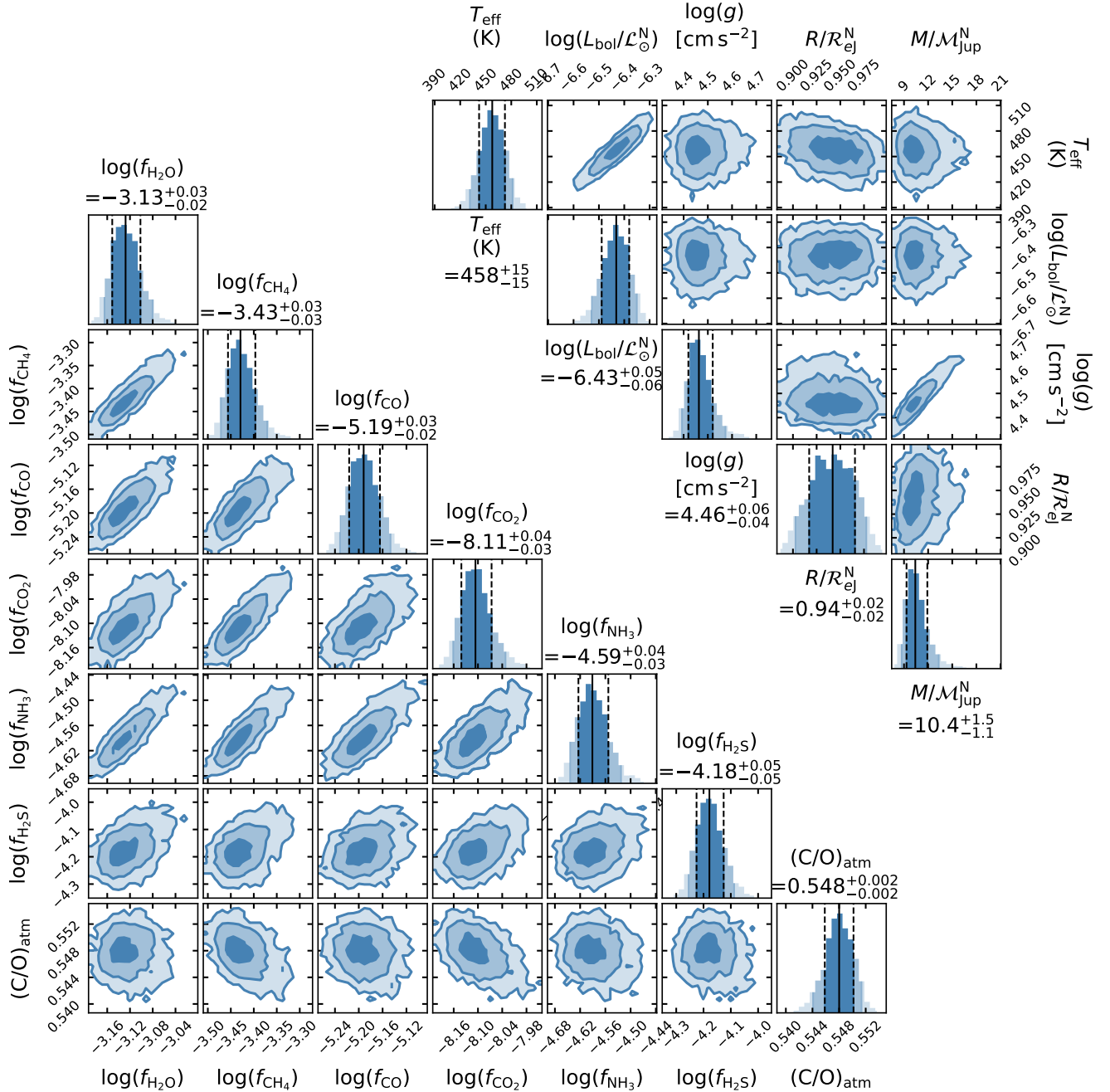


Figure 4. Lower left: Marginalized posterior probability distributions for H_2O , CH_4 , CO , CO_2 , NH_3 , H_2S , and atmospheric $(\text{C/O})_{\text{atm}}$ from the 5-knot retrieval for WISE 0359–54. **Upper right:** Marginalized posterior probability distributions for T_{eff} , L_{bol} , $\log(g)$, R_{ej}^{N} and $M_{\text{Jup}}^{\text{N}}$ from the 5-knot retrieval for WISE 0359–54. In both panels, the values above the histograms represent the parametric median (50th percentile) values with the errors representing the 1 σ (16th and 84th percentile) values. The different shades in the 1D and 2D histograms represent the 1, 2 and 3 σ central credible interval, respectively, with the darkest shade corresponding to 1 σ .

gley & Lodders 1996; Lodders 1999, 2002, 2010; Lodders & Fegley 2002; Lodders & Fegley 2006; Visscher et al. 2006; Visscher et al. 2010; Visscher 2012; Moses et al. 2013) at solar metallicity and C/O. The retrieved values are uniform-with-altitude and so show no variation

with pressure, while the model predictions are calculated along the retrieved thermal profile (see §4.1) and so do show variations with pressure. The rapid decrease in the model mixing ratios of H_2O , H_2S , and NH_3 above $\sim 10^{-2}$ bar are a result of these species condensing out of

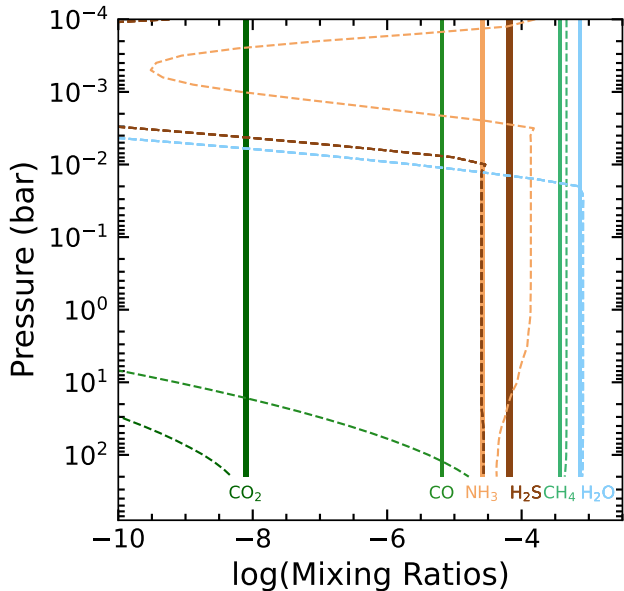


Figure 5. Retrieved uniform-with-altitude median mixing ratios with 1σ central credible interval (shaded) for H_2O , CH_4 , CO , CO_2 , NH_3 , and H_2S for WISE 0359–54 from the 5-knot retrieval. Also shown are the predicted thermochemical equilibrium mixing ratios (dashed).

the gas phase into water ice, ammonia ice, and NH_4SH (solid). The rapid increase in the mixing ratio of NH_3 above $10^{-3.2}$ bar is a result of the slight temperature reversal at the top of the thermal profile that is likely not physical (see §4.1).

The mixing ratio values of both H_2O and CH_4 indicate they are the most abundant species in the atmosphere and they agree well with the predictions. The NH_3 mixing ratio is 0.6 dex lower than the model predicts at the nominal pressure of 1 bar, while the mixing ratios of CO and CO_2 are orders of magnitude higher at 1 bar. All three of these mismatches can be ascribed to disequilibrium chemistry due to vertical mixing in the atmosphere (Fegley & Lodders 1996; Saumon et al. 2000; Hubeny & Burrows 2007a). We defer a discussion of this disequilibrium chemistry to §4.5 where we attempt to measure the vigor of this mixing using the retrieved mixing ratios and a 1D chemical kinetics forward modeling framework. Finally, the mixing ratio of H_2S is 0.4 dex ($2.5\times$) higher than the model predicts.

4.4. Physical properties: M , R , L_{bol} , g , and T_{eff}

The marginalized posterior distributions for M and R are shown in Figure 4. The M and R posterior samples can be used to calculate the posterior distribution for surface gravity ($g = MG/R^2$) and so the distribution of $\log(g)$ [cm s^{-2}] is also shown in Figure 4. The bolometric flux F_{bol} distribution can be calculated by integrat-

ing model spectra over all wavelengths. To account for light emerging at wavelengths shorter than $0.96 \mu\text{m}$ and longer than $12.0 \mu\text{m}$, we linearly interpolated the model from $0.96 \mu\text{m}$ to zero flux at zero wavelength and then extended the model to $\lambda = \infty$ using a Rayleigh-Jeans tail where $f_{\lambda,\text{RJ}} \propto \lambda^{-4}$; the constant of proportionality is calculated using the flux density of the last model wavelength. The bolometric luminosity is then given by $L_{\text{bol}} = 4\pi d^2 F_{\text{bol}}$, where d is the retrieved distance to the object, which results in the posterior distribution of $\log(L_{\text{bol}}/\mathcal{L}_{\odot}^{\text{N}})$ shown in Figure 4. Finally, we compute the effective temperature distribution shown in Figure 4 using the L_{bol} and R values and the Stefan-Boltzman Law,

$$T_{\text{eff}} = \left(\frac{L_{\text{bol}}}{4\pi\sigma R^2} \right)^{\frac{1}{4}}. \quad (7)$$

The retrieved mass of WISE 0359–54 is $10.4_{-1.1}^{+1.5} \mathcal{M}_{\text{Jup}}^{\text{N}}$, where $\mathcal{M}_{\text{Jup}}^{\text{N}}$ is the nominal Jupiter mass (assuming $G = 6.67430 \times 10^{-11} \text{ m}^3 \text{ kg}^{-1} \text{ s}^{-2}$, Mamajek et al. 2015). This value falls at the lower end of the ~ 9 – $31 \mathcal{M}_{\text{Jup}}^{\text{N}}$ range reported in Beiler et al. (2023) who used the observed bolometric luminosity of WISE 0359–54, an assumed age range of 1–10 Gyr, and the Sonora Bobcat solar metallicity evolutionary models (Marley et al. 2021) to estimate the mass of WISE 0359–54.

The retrieved radius is found to be $0.94 \pm 0.02 \mathcal{R}_{eJ}^{\text{N}}$, where $\mathcal{R}_{eJ}^{\text{N}}$ is Jupiter’s nominal equatorial radius of $7.1492 \times 10^7 \text{ m}$ (Mamajek et al. 2015). This is consistent with the value reported by Beiler et al. (2023) who used the observed bolometric luminosity of WISE 0359–54, an assumed age range of 1–10 Gyr, and the Sonora Bobcat solar metallicity evolutionary models (Marley et al. 2021) to find $0.94_{-0.057}^{+0.074} \mathcal{R}_{eJ}^{\text{N}}$ from a Monte Carlo simulation.

The bolometric luminosity of $\log(L_{\text{bol}}/\mathcal{L}_{\odot}^{\text{N}}) = -6.43_{-0.06}^{+0.05}$ is similar to the value of $\log(L_{\text{bol}}/\mathcal{L}_{\odot}^{\text{N}}) = -6.400 \pm 0.025$ reported by Beiler et al. (2023).

The retrieved surface gravity is $\log g = 4.46_{-0.04}^{+0.06} [\text{cm s}^{-2}]$ and the retrieved effective temperature is $T_{\text{eff}} = 458_{-15}^{+15} \text{ K}$. Figure 6 shows cloudless evolutionary models in the effective temperature/surface gravity plane with the position of WISE 0359–54 indicated. The loci of points with bolometric luminosities equal to that of WISE 0359–54 for ages between 0.1 and 10 Gyr is shown as a near-vertical line. The discrepancy between the two is most likely a result of the fact that the model does not extend to infinite wavelengths and thus our bolometric flux is systematically low. Also plotted is the best-fit effective temperature and surface gravity from Beiler et al. (2023) who used a custom grid of Sonora Cholla models (Karalidi et al. 2021) that includes an additional pa-

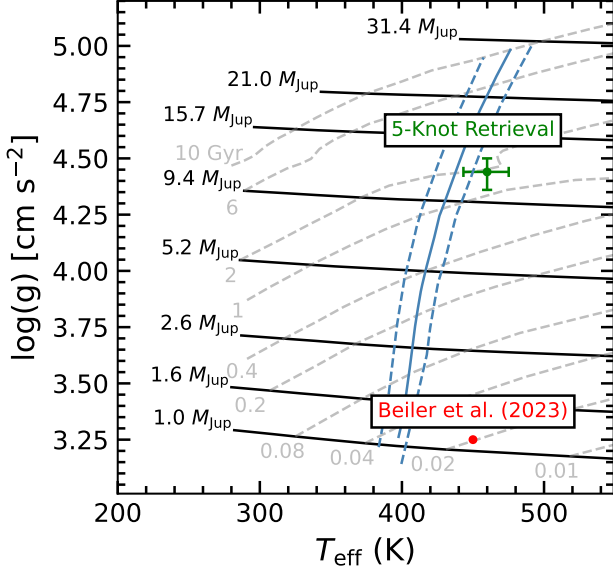


Figure 6. Evolution of Bobcat Sonora solar metallicity cloudless brown dwarfs in the effective temperature surface gravity plane (Marley et al. 2021). The black lines are cooling tracks for brown dwarfs with masses of 31.4, 21, 15.7, 9.4, 5.2, 2.6, 1.6 and $1 M_{\text{Jup}}^N$, while the gray lines are isochrones for ages of 10, 6, 2, 1, 0.4, 0.2, 0.08, 0.04, 0.02, and 0.01 Gyr. The loci of points with bolometric luminosities equal to that of WISE 0359-54 for ages between 0.1 and 10 Gyr are shown as the solid near-vertical lines while the $\pm 1\sigma$ uncertainties on the bolometric luminosities are shown as dotted lines. The blue dot shows the T_{eff} and $\log(g)$ value calculated using the 5-knot retrieved results with the horizontal and vertical error bar representing 1σ interval for T_{eff} and $\log(g)$, respectively. The red dot is the best-fit Sonora Bobcat model in Beiler et al. (2023)

parameter K_{zz} , the vertical eddy diffusion coefficient. The Beiler et al. surface gravity is uncomfortably low resulting in an age estimate of ~ 20 Myr. Our retrieved values gives an age of ~ 2 Gyr which is more consistent with the age estimates of the field population of warmer brown dwarfs (Dupuy & Liu 2017; Best et al. 2024).

4.5. Constraints on the eddy diffusion parameter- K_{zz}

Vertical atmospheric dynamics can significantly alter the photospheric abundance of gases like CH_4 , NH_3 , CO , and CO_2 by dredging them up from the hotter deeper atmosphere across several pressure scale heights. Exactly how much of the photospheric abundances are disturbed away from thermochemical equilibrium depends on the vigor of vertical mixing in the atmosphere of these objects (Fegley & Lodders 1994; Hubeny & Burrows 2007b; Visscher & Moses 2011; Zahnle & Marley 2014; Phillips et al. 2020; Karalidi et al. 2021; Mukherjee et al. 2022; Lacy & Burrows 2023; Lee et al. 2023). The strength of

vertical mixing is often quantified using the vertical eddy diffusion parameter- K_{zz} . The K_{zz} parameter quantifies the rate of overturning motion occurring in the atmosphere and a higher K_{zz} represents more vigorous vertical mixing. But K_{zz} has remained uncertain (even in the solar system giants) by several orders of magnitude until now mainly because of the lack of access to high SNR spectra of brown dwarfs in the infrared which can facilitate very precise constraints on atmospheric chemical abundances. The very precise constraints on abundances of various gases obtained in this work makes it a perfect target to constrain K_{zz} in its deep atmosphere.

In order to obtain constraints on K_{zz} from our retrieved gas abundances, we use the chemical kinetics model *Photochem* (Wogan et al. 2023). We use the median retrieved 5-knot thermal profile as an input to the chemical kinetics model along with the median $\log(g)$ constraints obtained by our 5-knot retrieval model. Using these inputs, we generate a grid of chemical forward models with *Photochem* by varying three key parameters that can influence chemistry of brown dwarfs – atmospheric metallicity, atmospheric $(\text{C}/\text{O})_{\text{atm}}$ ratio, and K_{zz} . For a given $(\text{C}/\text{O})_{\text{atm}}$, we remove about 20% of the O- from gas phase assuming it is used up in condensates in the deeper atmosphere. Our chemical forward model grid samples metallicities from sub-solar to super-solar values between -0.3 to $+0.3$ with an increment of 0.1 dex except between -0.2 to $+0.1$, for which the increment is even smaller at 0.02 dex. We also vary the $(\text{C}/\text{O})_{\text{atm}}$ ratio from sub-solar to super-solar values of 0.5 to $1.5 \times (\text{C}/\text{O})_{\odot}$, where the $(\text{C}/\text{O})_{\odot}$ is assumed to be 0.458. We vary $\log(K_{\text{zz}})$ from 2 to 11 with an increment of 1 except between the values of 6 to 10 where we include a finer sampling of 0.5. These K_{zz} values are in $\text{cm}^2 \text{ s}^{-1}$.

We use the extensive grid of chemical forward models to fit the retrieved abundances with the model abundance profiles of CH_4 , CO , CO_2 , H_2O , and NH_3 at a pressure of 0.1 bars. We choose this pressure because it is smaller than the minimum quench pressures expected for these gases for the range of K_{zz} used in this work. For each forward model, we define a combined χ^2 using,

$$\chi^2 = \sum_X \left(\frac{X_{\text{ret}} - X_{\text{model}}(0.1\text{bar})}{\sigma_{\text{ret}}^X} \right)^2 \quad (8)$$

where X_{ret} is the retrieved abundance of gas X , $X_{\text{model}}(0.1\text{bar})$ is the abundance of the same gas at 0.1 bars in the forward model grid, and σ_{ret}^X is the retrieved uncertainty on the abundance of gas X . We calculate the χ^2 of all our chemical models using this formulation and then produce a corner-plot for the sampled param-

ter points in our grid using $w=e^{-\chi^2/2}$ as weight for each sampled grid point.

Figure 7 shows this corner plot depicting our constraints on the atmospheric metallicity, $(C/O)_{\text{atm}}$ ratio, and K_{zz} obtained from the $T(P)$ profile and abundances retrieved using the 5-knot modeling setup. The best-fit forward model abundance profiles for CH_4 , CO , CO_2 , H_2O , and NH_3 along with the retrieved abundances are shown in Figure 8. This analysis finds that the atmospheric metallicity of the object is very slightly sub-solar and the $(C/O)_{\text{atm}}$ ratio is ~ 0.48 . We note that 20% of the O- has been removed out of the gas phase which means that the actual bulk gas phase $(C/O)_{\text{bulk}}$ in the deep atmosphere in this best-fit model is ~ 0.58 .

The best-fit K_{zz} value is found to be $10^9 \text{ cm}^2\text{s}^{-1}$, which is relatively large compared to previous estimates of K_{zz} in the atmospheres of cool brown dwarfs (Miles et al. 2020). Figure 8 shows that CH_4 and CO quench at ~ 10 bars in this best-fit case. This best-fit K_{zz} value is slightly inconsistent with the K_{zz} vs. T_{eff} trend observed in Miles et al. (2020), where K_{zz} values continue to be low at $T_{\text{eff}} > 400$ K but shows a dramatic rise when $T_{\text{eff}} < 400$ K. Mukherjee et al. (2022) used atmospheric forward models with a self-consistent treatment of disequilibrium chemistry to theoretically explain this trend as a result of gases quenching in deep “sandwiched” radiative zones with low K_{zz} in objects with $500 \text{ K} < T_{\text{eff}} < 1000$ K. The models showed that objects colder than 500 K tended to have gases quenched in their deep convective zones and are expected to show higher K_{zz} values representative of convective mixing. This theoretical trend was also found to have a significant gravity dependence in Mukherjee et al. (2022) where objects with $\log(g) < 4.5$ were expected to show convective zone quenching of gases across $400 \text{ K} < T_{\text{eff}} < 1000$ K.

Given that our 5-knot retrievals show that our target has a T_{eff} of 458_{-15}^{+15} K and $\log(g)$ of $4.46_{-0.04}^{+0.06}$, our finding of a high K_{zz} makes it consistent with the trend predicted in Mukherjee et al. (2022). Therefore, it is likely that we are probing the deep convective zone K_{zz} in this object and not the radiative zone or “sandwiched” radiative zone K_{zz} , as expected from self-consistent forward model trends. The maximum K_{zz} in the deep convective atmosphere of a brown dwarf with T_{eff} of 458 K and $\log(g)=4.46$ is $4.55 \times 10^{10} \text{ cm}^2\text{s}^{-1}$, calculated using Equation 4 in Zahnle & Marley (2014). This maximum K_{zz} in the convective zone is achieved when the entire energy flux from the interior is only carried out through convection in the deep atmosphere. However, in reality the interior energy flux is expected to be only partly carried out through convective transport and partly by radiative energy transport. In that case, the K_{zz} in the

convective atmosphere is expected to be lower than this upper limit. Figure 8 also shows that our model fitting approach fits the abundances of all these gases quite satisfactorily except for NH_3 . This might be suggestive of a slightly lower N/H ratio in the object than the scaled solar N/H ratio.

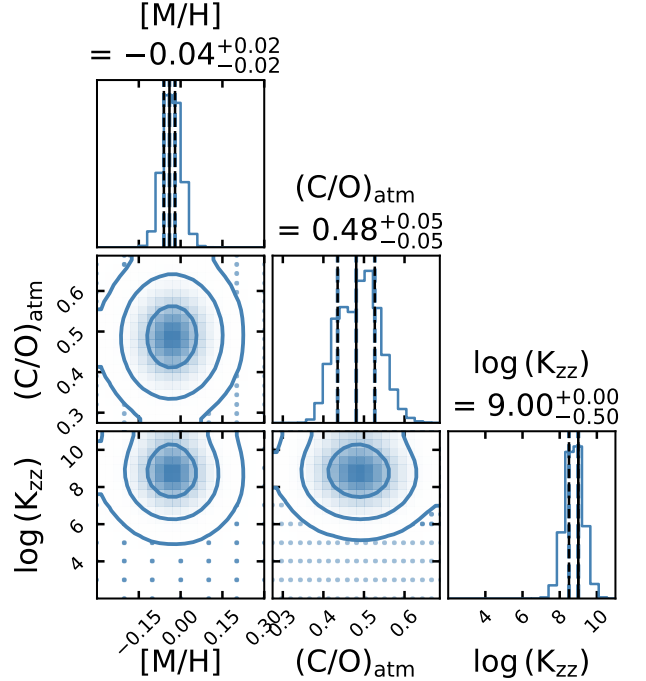


Figure 7. Corner plot showing the constraints on metallicity $[M/H]$, $(C/O)_{\text{atm}}$, and K_{zz} obtained by fitting the retrieved gaseous abundances of CH_4 , CO , NH_3 , H_2O , and CO_2 with a grid of disequilibrium chemistry forward models. The grid of disequilibrium chemistry forward models uses the retrieved 5-knot $T(P)$ profile constraint as an input and calculates the chemical abundance profiles across a large range of metallicity, $(C/O)_{\text{atm}}$, and K_{zz} . Gaseous abundances obtained in the 5-knot retrieval were used for this analysis.

4.6. Sensitivity to Thermal Profile Model

In order to quantify whether our choice of thermal profile model impacts the resulting mixing ratios, we ran a second retrieval using the parametric thermal profile model described in Madhusudhan & Seager (2009, hereafter M&S). In this model, the atmosphere is divided into three layers, for which the temperature and pressure are related by,

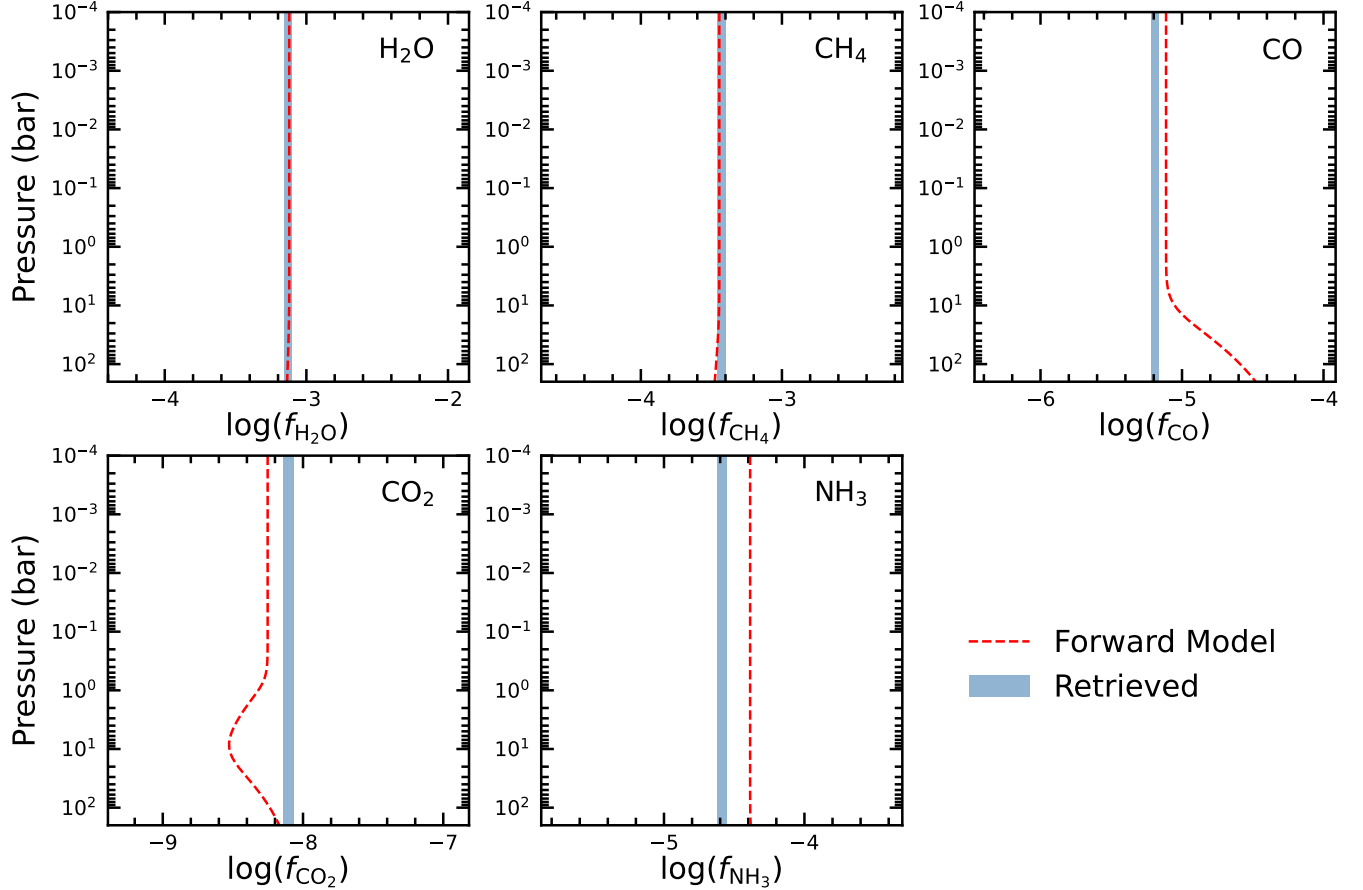


Figure 8. Comparison of the abundances in the best-fit disequilibrium chemistry forward model from *Photochem* with the retrieved abundances from the 5-knot thermal profile. Retrieved volume mixing ratios of CH_4 , CO , NH_3 , H_2O , and CO_2 are shown with blue shaded regions (representing 1σ central credible interval) in each panel, whereas the red lines show the profiles from the best-fit forward model.

$$P_0 < P < P_1 = P_0 e^{\alpha_1(T-T_0)^{1/2}} \quad (\text{Layer 1}) \quad (9)$$

$$P_1 < P < P_2 = P_2 e^{\alpha_2(T-T_2)^{1/2}} \quad (\text{Layer 2}) \quad (10)$$

$$P_3 < P = T_3 \quad (\text{Layer 3}), \quad (11)$$

where P_0 and T_0 are the pressure and temperature at the top of the atmosphere, respectively. We eliminate the possibility of a thermal inversion in the atmosphere by setting $P_2 = P_1$ and so we are left with 5 parameters: α_1 , α_2 , P_1 , P_3 , and T_3 , the priors of which are given Table 1. In the appendix, Figure 13 shows the marginalized posterior probability distributions for all 19 parameters and Table 3 gives the median, and 1σ uncertainty for each of the parameters.

The left panel of Figure 9 shows a comparison between the retrieved 5-knot thermal profile discussed in §4.1 and the M&S thermal profile while the right panel of Figure 9 shows the differences between the two. The profiles

agree within the uncertainties except below a pressure of a bar where the 5-knot profile is hotter by up to 100 K.

Figure 10 shows a comparison between the posterior distributions of the 12 parameters shown in Figure 4 ($f_{\text{H}_2\text{O}}$, f_{CH_4} , f_{CO} , f_{CO_2} , f_{NH_3} , $f_{\text{H}_2\text{S}}$, M , R , $(\text{C/O})_{\text{atm}}$, $\log g$, L_{bol} , and T_{eff}) from the 5-knot (blue) and the M&S (green) retrieval. Overall the agreement between the distributions is good (see also Table 3) which suggests our results are not strongly dependent on the underlying thermal profile model. The largest differences are for the distributions of M and $\log(f_{\text{H}_2\text{S}})$ with fractional differences of -0.64 and -0.10 , respectively.

Figure 11 shows the retrieved median model spectrum from the M&S retrieval (black) along with the 1σ central credible interval (red) and the retrieved median model spectrum from the 5-knot retrieval (green); the lower panel shows the residual between the two models. There

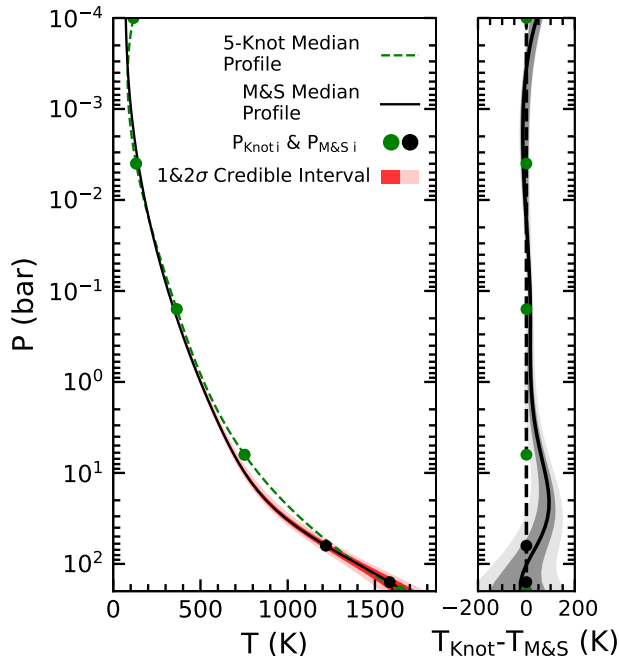


Figure 9. **Left panel:** shows the comparison between the two retrieved thermal profiles, where the black solid curve is the median M&S thermal profile, the red region shows the 1 and 2 σ confidence interval around the median profile, and the green curve is the 5-knot median thermal profile. **Right panel:** shows the difference between the the 5-knot and the M&S median profile, and the 1 and 2 σ central credible intervals, respectively.

5-knot profile predicts systematically higher fluxes in the J -, H -, and K -band opacity holes at 1.25, 1.6, and 2.1 μm and systematically lower fluxes between 5 and 7 μm . However, the median M&S retrieval predicts a higher flux in the Y -band ($\sim 1 \mu\text{m}$); this may be a result of the increased retrieved abundance of Na and K (0.26 and 0.04 dex larger, respectively) which forces light that would otherwise escape at wavelengths shorter than 1 μm to instead emerge in the Y -band opacity hole.

We chose nested sampling to sample posterior values due to its inherent ability to estimate the evidence, $p(\mathbf{D})$. We can compute the posterior odds ratio between the 5-knot model and the M&S model as,

$$\frac{p(5\text{-knot}|\mathbf{D})}{p(\text{M\&S}|\mathbf{D})} = \frac{p(5\text{-knot})}{p(\text{M\&S})} \frac{p(\mathbf{D}|5\text{-knot})}{p(\mathbf{D}|p(\Theta_{\text{M\&S}}))} \quad (12)$$

where the first term on the right-hand side is known as the prior odds and the last term on the right-hand side is known as the Bayes factor. Assuming the prior odds ratio is unity, the posterior odds is simply given by the Bayes factor

$$B_m = \frac{p(\mathbf{D}|p(\Theta_{5\text{-Knot}}))}{p(\mathbf{D}|p(\Theta_{\text{M\&S}}))}. \quad (13)$$

With $\ln p(\mathbf{D})$ values of 23540.66 ± 0.37 and 23560.97 ± 0.36 for the 5-knot and M&S retrievals, respectively, we calculated a Bayes factor of 6.65×10^8 . Based on the Jeffreys' scale (Jeffreys 1998), this value suggest that the M&S thermal profile is strongly preferred over the 5-knot profile. We can convert this value to an equivalent “ σ ” significance as described in Benneke & Seager (2013) and find a value of 6.69 σ .

5. SUMMARY

In this work, we present an atmospheric retrieval analysis of the Y0 brown dwarf WISE 0359–54 using the low-resolution 0.96–12 μm JWST spectrum obtained using NIRSpec and MIRI. The cloudless retrieval was performed using the Brewster retrieval framework. We retrieved volume number mixing ratios for 9 gases: H_2O , CH_4 , CO , CO_2 , NH_3 , H_2S , K, Na, PH_3 . These retrieved mixing ratios are 3–5 \times more precise than the previous work done using the HST WFC3 data (Zalesky et al. 2019). Since we were able to constrain all the major carbon- and oxygen-bearing molecules, we found $(\text{C}/\text{O})_{\text{atm}}$ to be 0.548 ± 0.002 . Apart from constraining the chemical composition, we also found an order of magnitude improvement in the precision of the retrieved thermal profile, which can be attributed to the broad wavelength coverage of the JWST data.

Using the retrieved thermal profile and the calculated surface gravity, we generated a grid of forward models with varying metallicity $[\text{M}/\text{H}]$, $(\text{C}/\text{O})_{\text{atm}}$, and eddy diffusion coefficient (K_{zz}) which tells the atmospheric mixing vigor. Comparing these generated models with our retrieved mixing ratios of H_2O , CH_4 , CO , CO_2 and NH_3 , we found strong evidence of vertical mixing in the atmosphere of WISE 0359–54 with a value of $K_{zz} = 10^9 \text{ [cm}^2\text{s}^{-1}\text{]}$.

Finally, to test the sensitivity of our results to our 5-knot thermal profile model, we performed another retrieval using the Madhusudhan & Seager (2009) thermal profile model. We found that the mixing ratios from both thermal profile model yield similar results (with the exception of $f_{\text{H}_2\text{S}}$ which is -0.10 dex lower) and that the retrieved thermal profile is similar except near the 5 bar pressure level where it is ~ 100 K hotter. Taken together, these results underscore the power that the James Webb Space Telescope has to study the atmospheres of the coolest brown dwarfs.

6. ACKNOWLEDGEMENT

This work is based [in part] on observations made with the NASA/ESA/CSA James Webb Space Tele-

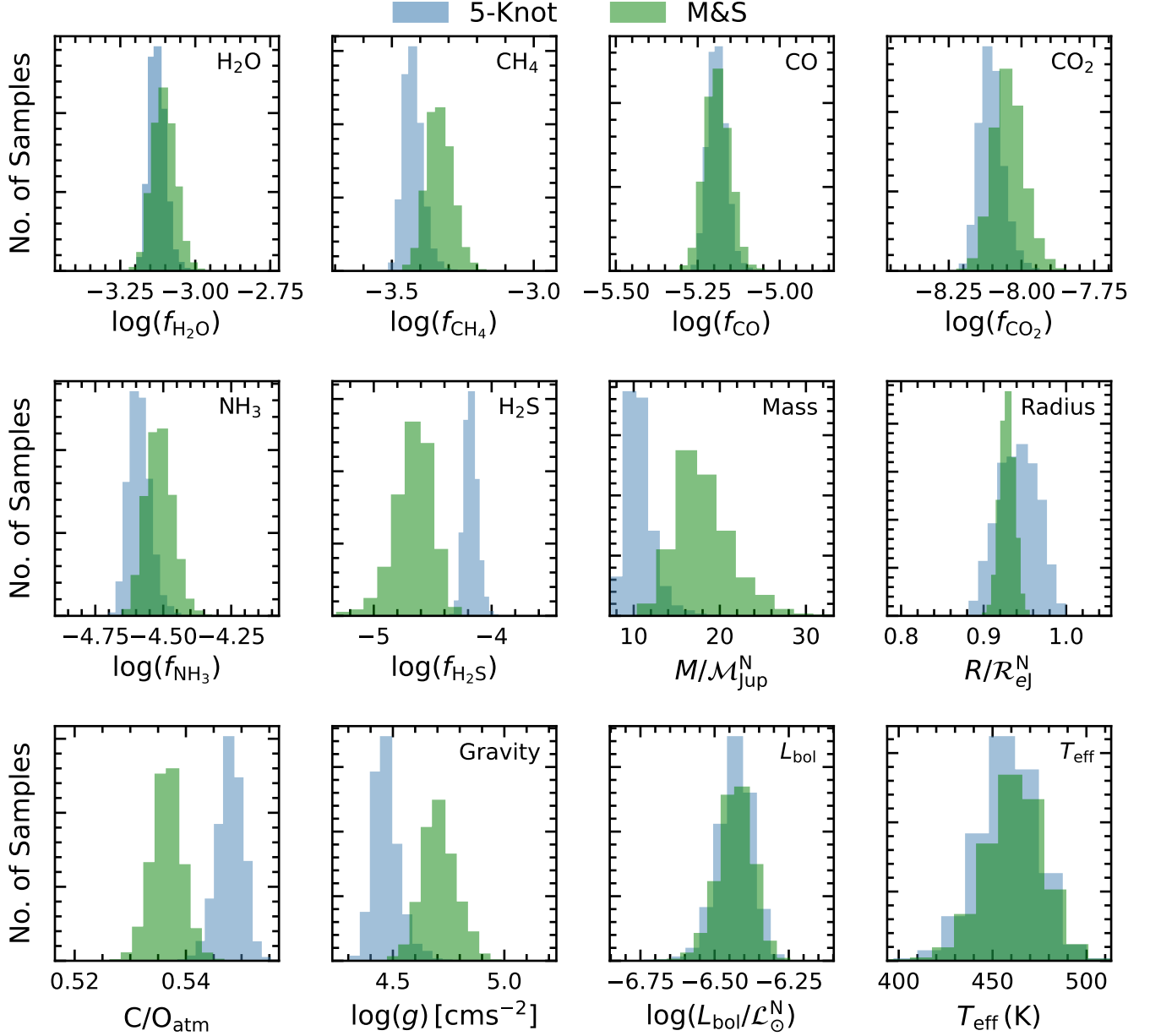


Figure 10. The posterior distributions retrieved for H_2O , CH_4 , CO , CO_2 , NH_3 , H_2S , mass, and radius alongside the calculated properties like $(\text{C/O})_{\text{atm}}$, gravity, L_{bol} , and T_{eff} from the 5-knot (blue) and M&S (green) retrieval.

scope. These observations are associated with program #2302.

This research has made use of the SIMBAD database, operated at CDS, Strasbourg, France.

We would also like to thank Jacqueline K. Faherty and Channon Visscher for their valuable insight on the retrieved results and the working of the chemistry in such cold objects.

Software: Corner (Foreman-Mackey 2016), Matplotlib (Hunter 2007), Numpy (Harris et al. 2020)

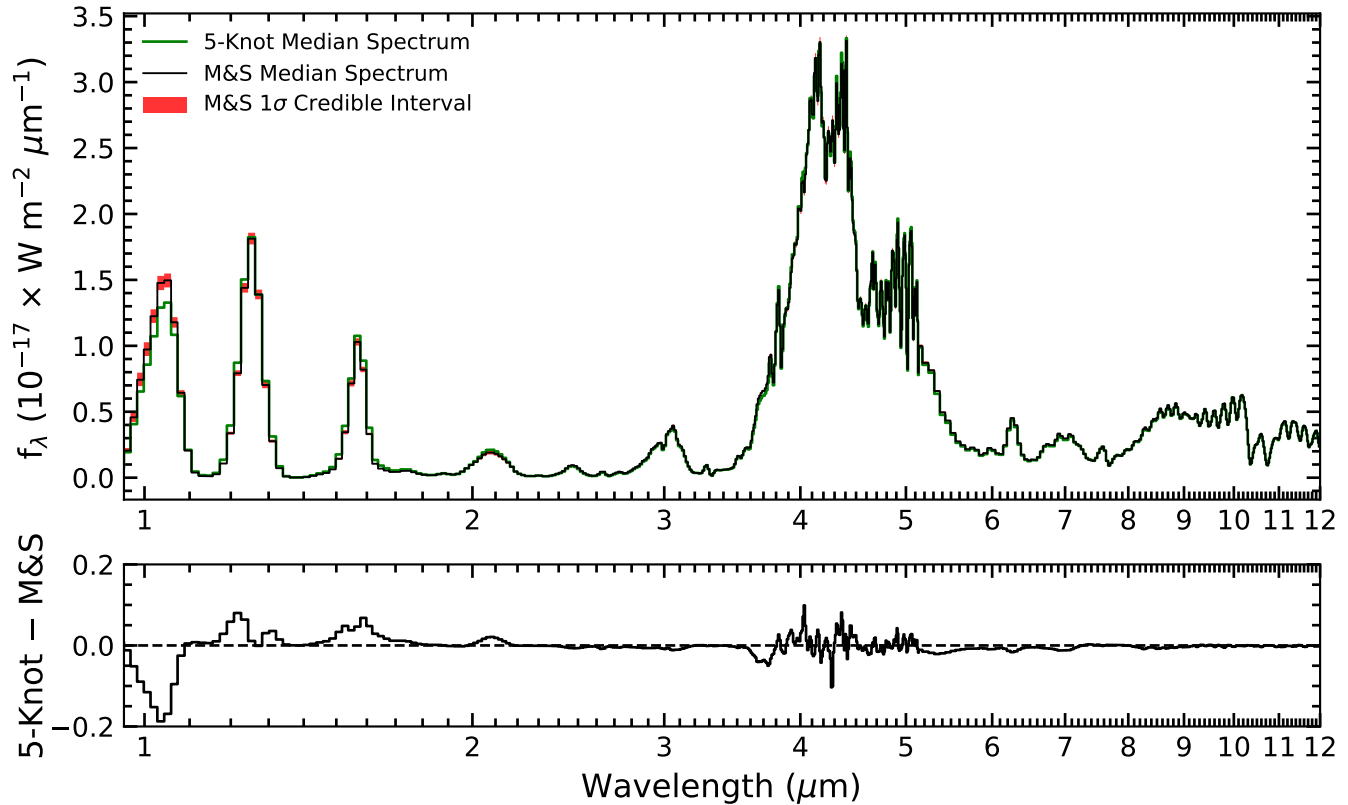


Figure 11. The top panel of the figure shows the retrieved median spectrum from M&S retrieval in black and the retrieved median spectrum from 5-knot retrieval in green for WISE 0359–54 spectrum covering 0.96–12 μ m. The red region shows the 1 σ region around the M&S median spectrum. The bottom panel of the figure shows the residual spectrum calculated by taking the difference between the retrieved M&S median spectrum and the retrieved 5-knot median spectrum.

REFERENCES

- Adams, A. D., Meyer, M. R., Howe, A. R., et al. 2023, Atmospheric Retrieval of L Dwarfs: Benchmarking Results and Characterizing the Young Planetary Mass Companion HD 106906 b in the Near-Infrared. <https://arxiv.org/abs/2309.10188>
- Asplund, M., Grevesse, N., Sauval, A. J., & Scott, P. 2009, *ARA&A*, 47, 481, doi: 10.1146/annurev.astro.46.060407.145222
- Barrado, D., Mollière, P., Patapis, P., et al. 2023, *Nature*, 624, 263–266, doi: 10.1038/s41586-023-06813-y
- Barshay, S. S., & Lewis, J. S. 1978, *Icarus*, 33, 593, doi: [https://doi.org/10.1016/0019-1035\(78\)90192-6](https://doi.org/10.1016/0019-1035(78)90192-6)
- Beer, R. 1975, *ApJL*, 200, L167, doi: 10.1086/181923
- Beiler, S. A., Cushing, M. C., Kirkpatrick, J. D., et al. 2023, *The Astrophysical Journal Letters*, 951, L48, doi: 10.3847/2041-8213/ace32c
- Benneke, B., & Seager, S. 2013, *The Astrophysical Journal*, 778, 153, doi: 10.1088/0004-637x/778/2/153
- Best, W. M. J., Sanghi, A., Liu, M. C., Magnier, E. A., & Dupuy, T. J. 2024, arXiv e-prints, arXiv:2401.09535, doi: 10.48550/arXiv.2401.09535
- Bregman, J. D., Lester, D. F., & Rank, D. M. 1975, *ApJL*, 202, L55, doi: 10.1086/181979
- Buchner, J., Georgakakis, A., Nandra, K., et al. 2014, *A&A*, 564, A125, doi: 10.1051/0004-6361/201322971
- Burningham, B., Marley, M. S., Line, M. R., et al. 2017, *MNRAS*, 470, 1177, doi: 10.1093/mnras/stx1246
- Center, O. S. 1987, Ohio Supercomputer Center. <http://osc.edu/ark:/19495/f5s1ph73>
- . 2016, Owens Supercomputer. <http://osc.edu/ark:/19495/hpc6h5b1>
- Chahine, M. T. 1968, *Journal of the Optical Society of America* (1917-1983), 58, 1634
- Chamberlain, J. W., & Hunten, D. M. 1987, *Theory of planetary atmospheres. An introduction to their physics and chemistry.*, Vol. 36

Table 3. Posterior Parametric Values

Parameter	5-Knot Retrieval ^a	M&S Retrieval ^a	Fractional Difference ^b
$\log(f_{\text{H}_2\text{O}})$	$-3.13^{+0.03}_{-0.02}$	$-3.10^{+0.04}_{-0.04}$	$0.01^{+0.01}_{-0.01}$
$\log(f_{\text{CH}_4})$	$-3.43^{+0.03}_{-0.03}$	$-3.34^{+0.04}_{-0.04}$	$0.03^{+0.01}_{-0.01}$
$\log(f_{\text{CO}})$	$-5.19^{+0.03}_{-0.02}$	$-5.18^{+0.04}_{-0.04}$	$0.00^{+0.01}_{-0.01}$
$\log(f_{\text{CO}_2})$	$-8.11^{+0.04}_{-0.03}$	$-8.05^{+0.05}_{-0.05}$	$0.01^{+0.01}_{-0.01}$
$\log(f_{\text{NH}_3})$	$-4.59^{+0.04}_{-0.03}$	$-4.51^{+0.05}_{-0.05}$	$0.02^{+0.01}_{-0.01}$
$\log(f_{\text{H}_2\text{S}})$	$-4.18^{+0.05}_{-0.05}$	$-4.60^{+0.12}_{-0.12}$	$-0.10^{+0.03}_{-0.03}$
$\log(f_{\text{K}})$	$-9.31^{+1.66}_{-1.68}$	$-8.96^{+1.86}_{-1.96}$	$0.03^{+0.23}_{-0.28}$
$\log(f_{\text{Na}})$	$-10.32^{+1.08}_{-1.07}$	$-7.45^{+0.16}_{-0.49}$	$0.26^{+0.08}_{-0.11}$
$\log(f_{\text{PH}_3})$	$-10.00^{+1.15}_{-1.26}$	$-10.22^{+1.17}_{-1.13}$	$-0.02^{+0.15}_{-0.17}$
$M/\mathcal{M}_{\text{Jup}}^{\text{N}}$	$10.40^{+1.50}_{-1.10}$	$17.20^{+2.80}_{-2.40}$	$-0.64^{+0.30}_{-0.34}$
$R/\mathcal{R}_{eJ}^{\text{N}}$	$0.94^{+0.02}_{-0.02}$	$0.93^{+0.01}_{-0.01}$	$0.01^{+0.03}_{-0.03}$
$\Delta\lambda$	$0.00^{+0.00}_{-0.00}$	$0.00^{+0.00}_{-0.00}$	$0.04^{+0.13}_{-0.14}$
$\log b$	$-37.04^{+0.04}_{-0.04}$	$-37.02^{+0.04}_{-0.04}$	$0.00^{+0.00}_{-0.00}$
d	$-13.66^{+0.33}_{-0.35}$	$-13.50^{+0.02}_{-0.03}$	$0.01^{+0.01}_{-0.01}$
$T_{\text{Knot } 1}$	$115.71^{+11.58}_{-13.26}$
$T_{\text{Knot } 2}$	$130.84^{+11.06}_{-7.23}$
$T_{\text{Knot } 3}$	$363.94^{+2.80}_{-3.14}$
$T_{\text{Knot } 4}$	$752.58^{+7.72}_{-9.52}$
$T_{\text{Knot } 5}$	$1734.47^{+28.94}_{-34.37}$
α_1	...	$0.45^{+0.00}_{-0.00}$...
α_2	...	$0.03^{+0.01}_{-0.01}$...
P_1	...	$1.79^{+0.10}_{-0.08}$...
P_3	...	$2.23^{+0.06}_{-0.08}$...
T_1	...	$2048.75^{+143.26}_{-161.03}$...

NOTE—^aAll mixing ratios are reported as the log of the volume mixing ratio (the amount of molecular gas out of the total amount of molecular gas), where the remainder of the gas is assumed to be H₂-He at a fixed solar ratio.

^b The difference between the 5-Knot and M&S retrieved posterior samples divided by the 5-Knot retrieved posterior samples.

Dupuy, T. J., & Liu, M. C. 2017, *The Astrophysical Journal Supplement Series*, 231, 15, doi: [10.3847/1538-4365/aa5e4c](https://doi.org/10.3847/1538-4365/aa5e4c)

Faherty, J., Burningham, B., Gagné, J., et al. 2024, in *AAS/Division for Extreme Solar Systems Abstracts*, Vol. 56, AAS/Division for Extreme Solar Systems Abstracts, 101.02

Fegley, B., & Lodders, K. 1994, *Icarus*, 110, 117, doi: <https://doi.org/10.1006/icar.1994.1111>

Fegley, Bruce, J., & Lodders, K. 1996, *ApJL*, 472, L37, doi: [10.1086/310356](https://doi.org/10.1086/310356)

Feroz, F., Hobson, M. P., & Bridges, M. 2009, *Monthly Notices of the Royal Astronomical Society*, 398, 1601–1614, doi: [10.1111/j.1365-2966.2009.14548.x](https://doi.org/10.1111/j.1365-2966.2009.14548.x)

Foreman-Mackey, D. 2016, *corner.py* on GitHub, <https://github.com/dfm/corner.py>

Foreman-Mackey, D., Conley, A., Meierjürgen Farr, W., et al. 2013, *emcee: The MCMC Hammer*, *Astrophysics Source Code Library*, record ascl:1303.002, <http://ascl.net/1303.002>

Gardner, J. P., Mather, J. C., Clampin, M., et al. 2006, *Space Science Reviews*, 123, 485–606, doi: [10.1007/s11214-006-8315-7](https://doi.org/10.1007/s11214-006-8315-7)

Gillett, F. C., Forrest, W. J., & Merrill, K. M. 1973, *ApJ*, 183, 87, doi: [10.1086/152211](https://doi.org/10.1086/152211)

Harris, C. R., Millman, K. J., van der Walt, S. J., et al. 2020, *Nature*, 585, 357–362, doi: [10.1038/s41586-020-2649-2](https://doi.org/10.1038/s41586-020-2649-2)

Hogg, D. W., Bovy, J., & Lang, D. 2010, *Data analysis recipes: Fitting a model to data*, <https://arxiv.org/abs/1008.4686>

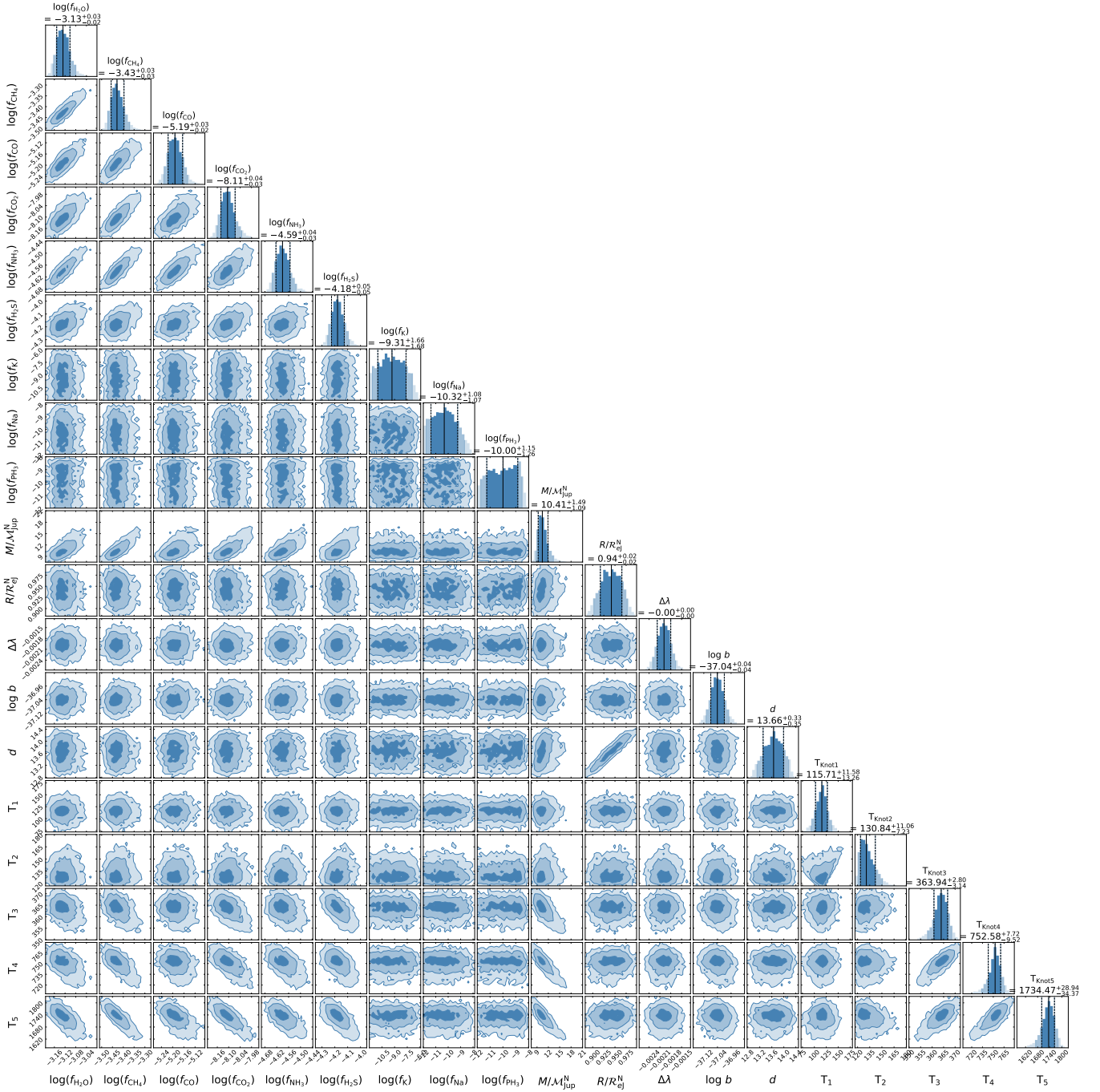


Figure 12. Marginalized posterior probability distributions for each parameter from the 5-knot retrieval for WISE 0359-54. The first 9 parameters represent the retrieved mixing ratios for H_2O , CH_4 , CO , CO_2 , NH_3 , H_2S , K , Na and PH_3 , followed by mass and radius. The parameters $\Delta\lambda$ and $\log b$ are nuisance parameters, d is the distance to the object, and the last five parameters are the retrieved temperature knots. The values above the 1-D histograms represent the parametric median (50th percentile) values with the errors representing the 1σ central credible interval (16th and 84th percentile) values. The different shades in the 1-D and 2-D histograms represent the 1, 2 and 3σ central credible interval, respectively, with the darkest shade corresponding to 1σ .

Hood, C. E., Fortney, J. J., Line, M. R., & Faherty, J. K. 2023, Brown Dwarf Retrievals on FIRE!: Atmospheric Constraints and Lessons Learned from High Signal-to-Noise Medium Resolution Spectroscopy of a T9 Dwarf. <https://arxiv.org/abs/2303.04885>

Hood, C. E., Mukherjee, S., Fortney, J. J., et al. 2024, High-Precision Atmospheric Constraints for a Cool T Dwarf from JWST Spectroscopy. <https://arxiv.org/abs/2402.05345>

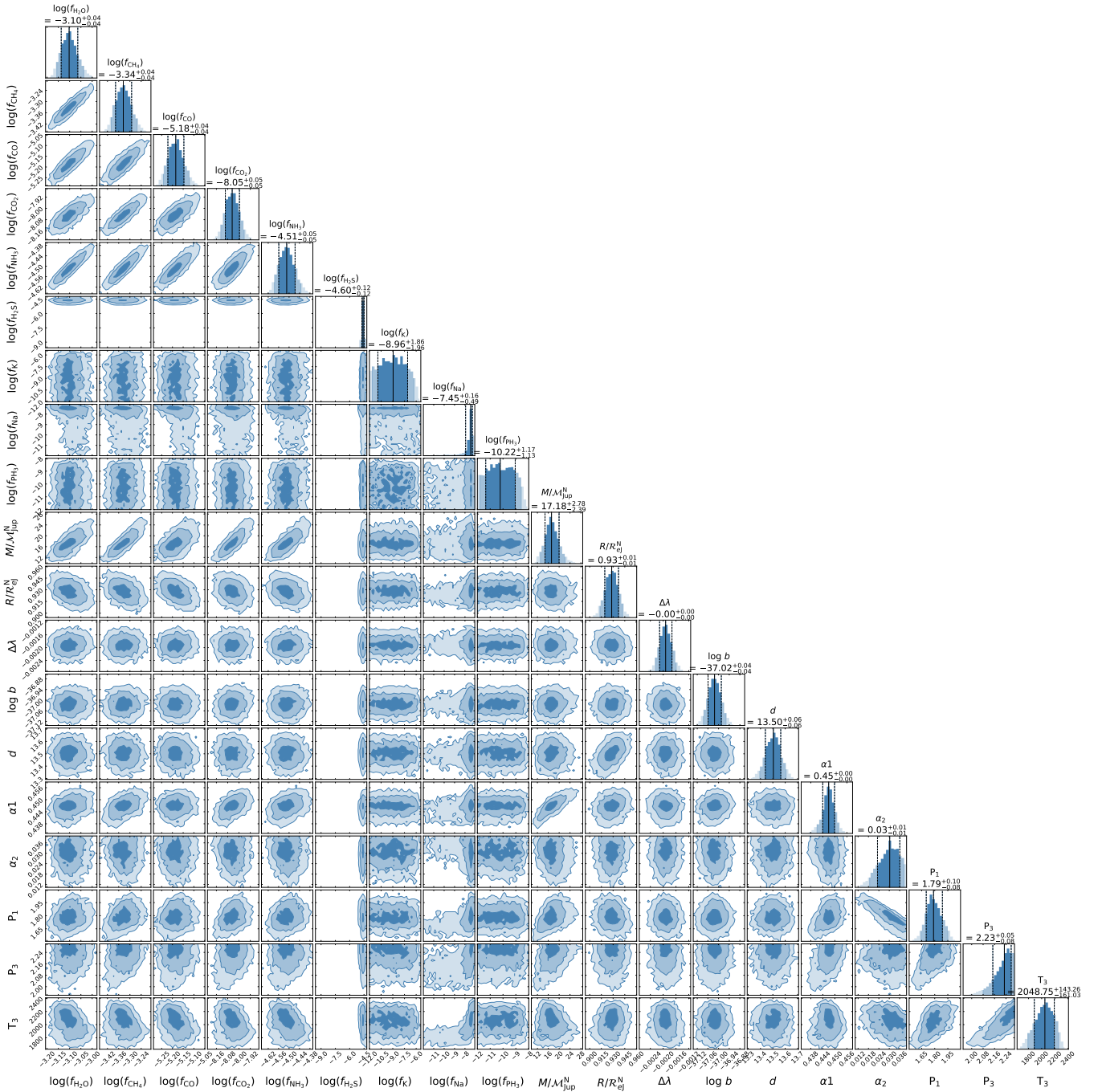


Figure 13. Marginalized posterior probability distributions for each parameter from the M&S retrieval for WISE 0359–54. The first 9 parameters represent the retrieved mixing ratios for H_2O , CH_4 , CO , CO_2 , NH_3 , H_2S , K , Na and PH_3 , followed by mass and radius. The parameters $\Delta\lambda$ and $\log b$ are nuisance parameters, d is the distance to the object, and the last five parameters are the retrieved temperature knots (points). The values above the 1-D histograms represent the parametric median (50th percentile) values with the errors representing the 1σ central credible interval (16th and 84th percentile) values. The different shades in the 1-D and 2-D histograms represent the 1, 2 and 3σ central credible interval, respectively, with the darkest shade corresponding to 1σ .

Hubeny, I., & Burrows, A. 2007a, ApJ, 669, 1248,

doi: [10.1086/522107](https://doi.org/10.1086/522107)

—. 2007b, ApJ, 659, 1458, doi: [10.1086/512179](https://doi.org/10.1086/512179)

Hunter, J. D. 2007, Computing in science and engineering,

9, 90, doi: [10.1109/MCSE.2007.55](https://doi.org/10.1109/MCSE.2007.55)

- Jakobsen, P., Ferruit, P., Alves de Oliveira, C., et al. 2022, *Astronomy & Astrophysics*, 661, A80, doi: [10.1051/0004-6361/202142663](https://doi.org/10.1051/0004-6361/202142663)
- Jeffreys, H. 1998, *The Theory of Probability*, Oxford Classic Texts in the Physical Sciences (OUP Oxford). <https://books.google.com/books?id=vh9Act9rtzQC>
- Karalidi, T., Marley, M., Fortney, J. J., et al. 2021, *The Astrophysical Journal*, 923, 269, doi: [10.3847/1538-4357/ac3140](https://doi.org/10.3847/1538-4357/ac3140)
- Karalidi, T., Marley, M., Fortney, J. J., et al. 2021, *ApJ*, 923, 269, doi: [10.3847/1538-4357/ac3140](https://doi.org/10.3847/1538-4357/ac3140)
- Kirkpatrick, D. J., Gelino, C. R., Cushing, M. C., et al. 2012, *The Astrophysical Journal*, 753, 156, doi: [10.1088/0004-637x/753/2/156](https://doi.org/10.1088/0004-637x/753/2/156)
- Kirkpatrick, J. D., Gelino, C. R., Faherty, J. K., et al. 2021, *The Astrophysical Journal Supplement Series*, 253, 7, doi: [10.3847/1538-4365/abd107](https://doi.org/10.3847/1538-4365/abd107)
- Lacy, B., & Burrows, A. 2023, *ApJ*, 950, 8, doi: [10.3847/1538-4357/acc8cb](https://doi.org/10.3847/1538-4357/acc8cb)
- Lee, E. K. H., Tan, X., & Tsai, S.-M. 2023, *MNRAS*, 523, 4477, doi: [10.1093/mnras/stad1715](https://doi.org/10.1093/mnras/stad1715)
- Lew, B. W. P., Roellig, T., Batalha, N. E., et al. 2024, High-precision atmospheric characterization of a Y dwarf with JWST NIRSpec G395H spectroscopy: isotopologue, C/O ratio, metallicity, and the abundances of six molecular species. <https://arxiv.org/abs/2402.05900>
- Line, M. R., Fortney, J. J., Marley, M. S., & Sorahana, S. 2014, *ApJ*, 793, 33, doi: [10.1088/0004-637X/793/1/33](https://doi.org/10.1088/0004-637X/793/1/33)
- Lodders, K. 1999, *ApJ*, 519, 793, doi: [10.1086/307387](https://doi.org/10.1086/307387)
- . 2002, *ApJ*, 577, 974, doi: [10.1086/342241](https://doi.org/10.1086/342241)
- Lodders, K. 2010, in *Astrophysics and Space Science Proceedings*, Vol. 16, Principles and Perspectives in Cosmochemistry, 379, doi: [10.1007/978-3-642-10352-0_8](https://doi.org/10.1007/978-3-642-10352-0_8)
- Lodders, K., & Fegley, B. 2002, *Icarus*, 155, 393, doi: [10.1006/icar.2001.6740](https://doi.org/10.1006/icar.2001.6740)
- Lodders, K., & Fegley, B. 2006, *Chemistry of Low Mass Substellar Objects* (Springer Berlin Heidelberg), 1–28, doi: [10.1007/3-540-30313-8_1](https://doi.org/10.1007/3-540-30313-8_1)
- Lueber, A., Kitzmann, D., Bowler, B. P., Burgasser, A. J., & Heng, K. 2022, *The Astrophysical Journal*, 930, 136, doi: [10.3847/1538-4357/ac63b9](https://doi.org/10.3847/1538-4357/ac63b9)
- Luhman, K. L., Tremblin, P., de Oliveira, C. A., et al. 2023, JWST/NIRSpec Observations of the Coldest Known Brown Dwarf. <https://arxiv.org/abs/2311.17316>
- Madhusudhan, N., & Seager, S. 2009, *ApJ*, 707, 24, doi: [10.1088/0004-637X/707/1/24](https://doi.org/10.1088/0004-637X/707/1/24)
- Madhusudhan, N., & Seager, S. 2009, *The Astrophysical Journal*, 707, 24–39, doi: [10.1088/0004-637x/707/1/24](https://doi.org/10.1088/0004-637x/707/1/24)
- Mamajek, E. E., Prsa, A., Torres, G., et al. 2015, IAU 2015 Resolution B3 on Recommended Nominal Conversion Constants for Selected Solar and Planetary Properties. <https://arxiv.org/abs/1510.07674>
- Marley, M. S., Saumon, D., Visscher, C., et al. 2021, *ApJ*, 920, 85, doi: [10.3847/1538-4357/ac141d](https://doi.org/10.3847/1538-4357/ac141d)
- Miles, B. E., Skemer, A. J. I., Morley, C. V., et al. 2020, *AJ*, 160, 63, doi: [10.3847/1538-3881/ab9114](https://doi.org/10.3847/1538-3881/ab9114)
- Moses, J. I., Line, M. R., Visscher, C., et al. 2013, *ApJ*, 777, 34, doi: [10.1088/0004-637X/777/1/34](https://doi.org/10.1088/0004-637X/777/1/34)
- Mukherjee, S., Fortney, J. J., Batalha, N. E., et al. 2022, *ApJ*, 938, 107, doi: [10.3847/1538-4357/ac8dfb](https://doi.org/10.3847/1538-4357/ac8dfb)
- Mukherjee, S., Fortney, J. J., Morley, C. V., et al. 2024, The Sonora Substellar Atmosphere Models. IV. Elf Owl: Atmospheric Mixing and Chemical Disequilibrium with Varying Metallicity and C/O Ratios. <https://arxiv.org/abs/2402.00756>
- Phillips, M. W., Tremblin, P., Baraffe, I., et al. 2020, *A&A*, 637, A38, doi: [10.1051/0004-6361/201937381](https://doi.org/10.1051/0004-6361/201937381)
- Rieke, G. H., Ressler, M. E., Morrison, J. E., et al. 2015, *PASP*, 127, 665, doi: [10.1086/682257](https://doi.org/10.1086/682257)
- Rowland, M. J., Morley, C. V., & Line, M. R. 2023, *The Astrophysical Journal*, 947, 6, doi: [10.3847/1538-4357/acbb07](https://doi.org/10.3847/1538-4357/acbb07)
- Saumon, D., Geballe, T. R., Leggett, S. K., et al. 2000, *The Astrophysical Journal*, 541, 374–389, doi: [10.1086/309410](https://doi.org/10.1086/309410)
- Schneider, A. C., Cushing, M. C., Kirkpatrick, J. D., et al. 2015, *ApJ*, 804, 92, doi: [10.1088/0004-637X/804/2/92](https://doi.org/10.1088/0004-637X/804/2/92)
- Speagle, J. S. 2020, *Monthly Notices of the Royal Astronomical Society*, 493, 3132–3158, doi: [10.1093/mnras/staa278](https://doi.org/10.1093/mnras/staa278)
- Tannock, M. E., Metchev, S., Hood, C. E., et al. 2022, *Monthly Notices of the Royal Astronomical Society*, 514, 3160, doi: [10.1093/mnras/stac1412](https://doi.org/10.1093/mnras/stac1412)
- Toon, O. B., McKay, C. P., Ackerman, T. P., & Santhanam, K. 1989, *J. Geophys. Res.*, 94, 16287, doi: [10.1029/JD094iD13p16287](https://doi.org/10.1029/JD094iD13p16287)
- Visscher, C. 2012, *The Astrophysical Journal*, 757, 5, doi: [10.1088/0004-637x/757/1/5](https://doi.org/10.1088/0004-637x/757/1/5)
- Visscher, C., Lodders, K., & Fegley, Jr., B. 2006, *The Astrophysical Journal*, 648, 1181–1195, doi: [10.1086/506245](https://doi.org/10.1086/506245)
- Visscher, C., Lodders, K., & Fegley, Bruce, J. 2010, *ApJ*, 716, 1060, doi: [10.1088/0004-637X/716/2/1060](https://doi.org/10.1088/0004-637X/716/2/1060)
- Visscher, C., & Moses, J. I. 2011, *ApJ*, 738, 72
- Vos, J. M., Burningham, B., Faherty, J. K., et al. 2023, *ApJ*, 944, 138, doi: [10.3847/1538-4357/acab58](https://doi.org/10.3847/1538-4357/acab58)
- Wogan, N. F., Catling, D. C., Zahnle, K. J., & Lupu, R. 2023, *PSJ*, 4, 169, doi: [10.3847/PSJ/aced83](https://doi.org/10.3847/PSJ/aced83)

Zahnle, K. J., & Marley, M. S. 2014, ApJ, 797, 41,
doi: [10.1088/0004-637X/797/1/41](https://doi.org/10.1088/0004-637X/797/1/41)

Zalesky, J. A., Line, M. R., Schneider, A. C., & Patience, J.
2019, ApJ, 877, 24, doi: [10.3847/1538-4357/ab16db](https://doi.org/10.3847/1538-4357/ab16db)